

Imaging with terahertz radiation

Wai Lam Chan, Jason Deibel and Daniel M Mittleman

Department of Electrical and Computer Engineering, MS-366, Rice University,
6100 Main St., Houston, TX 77005, USA

E-mail: daniel@rice.edu

Received 9 January 2007, in final form 6 June 2007

Published 12 July 2007

Online at stacks.iop.org/RoPP/70/1325

Abstract

Within the last several years, the field of terahertz science and technology has changed dramatically. Many new advances in the technology for generation, manipulation, and detection of terahertz radiation have revolutionized the field. Much of this interest has been inspired by the promise of valuable new applications for terahertz imaging and sensing. Among a long list of proposed uses, one finds compelling needs such as security screening and quality control, as well as whimsical notions such as counting the almonds in a bar of chocolate. This list has grown in parallel with the development of new technologies and new paradigms for imaging and sensing. Many of these proposed applications exploit the unique capabilities of terahertz radiation to penetrate common packaging materials and provide spectroscopic information about the materials within. Several of the techniques used for terahertz imaging have been borrowed from other, more well established fields such as x-ray computed tomography and synthetic aperture radar. Others have been developed exclusively for the terahertz field, and have no analogies in other portions of the spectrum. This review provides a comprehensive description of the various techniques which have been employed for terahertz image formation, as well as discussing numerous examples which illustrate the many exciting potential uses for these emerging technologies.

(Some figures in this article are in colour only in the electronic version)

This article was invited by Professor K Ploog.

Contents

	Page
1. Introduction	1327
2. Diffraction-limited imaging with terahertz radiation	1329
2.1. Advantages and disadvantages of the time-domain approach	1330
2.2. Imaging with a time-domain spectrometer	1334
2.3. Time-of-flight imaging	1339
2.4. Depth resolution in time-of-flight imaging	1342
2.5. Tomography with terahertz radiation	1345
2.6. Video-rate terahertz imaging and single-shot terahertz imaging	1351
2.7. Terahertz imaging with a continuous-wave source	1353
2.8. Some more examples	1355
3. Terahertz imaging below the diffraction limit	1361
3.1. Terahertz near-field imaging with a sub-wavelength aperture	1362
3.2. Apertureless near-field terahertz imaging	1364
3.3. Terahertz spectroscopy and ANSOM	1366
3.4. Terahertz emission imaging	1370
4. Conclusions	1371
Acknowledgments	1372
References	1372

1. Introduction

The terahertz (THz) region of the electromagnetic spectrum lies in the gap between microwaves and infrared. This so-called ‘terahertz gap’ has historically been defined by the relative lack of convenient and inexpensive sources, detectors, and systems for terahertz waves. For frequencies below about 100 GHz (corresponding to a free-space wavelength of $\lambda = 3$ mm), electronic components can be purchased from a number of commercial suppliers, and millimetre-wave imaging systems are becoming available. Above 10 THz ($\lambda = 30$ μm), thermal (black-body) sources are an increasingly efficient means for generating radiation, thermal cameras are commercially available, and optical techniques are more readily applicable. The two orders of magnitude of frequency spectrum in between are, relatively speaking, much less well explored (see figure 1). Within the last 15 years, many new terahertz techniques have been pioneered, motivated in part by the vast range of possible applications for terahertz imaging, sensing, and spectroscopy [1]. The purpose of this review is to provide an up-to-date survey of the state of the art in the rapidly moving field of terahertz imaging.

Much of the interest in terahertz science and technology has grown out of the natural overlap between the electronics and optics points of view. Below the THz range, one typically detects the electric field of a propagating wave using an antenna, whereas at higher frequencies one generally speaks of the intensity or irradiance, proportional to the photon flux. In the optical and infrared range, photon energies and the relevant energy level spacings are generally much larger than or comparable to $k_{\text{B}}T$, the thermal energy at room temperature. In contrast, in the microwave regime, energy level spacings are smaller than $k_{\text{B}}T$, so one can generally neglect the quantized nature of the radiation field. The terahertz regime is therefore a natural bridge between the quantum mechanical and classical descriptions of electromagnetic waves and their interactions with materials. Additionally, microwave devices and systems often rely on propagation via guided waves, and one rarely encounters the collimated free-space beams that are the typical output of lasers. Many technological advances in the terahertz range have originated from the melding of these two very different viewpoints, borrowing ideas and concepts from each.

Naturally, the idea of using terahertz radiation for imaging and sensing, in analogy to the many similar applications of both optical and microwave radiation, has been discussed for at least several decades [2]. Early researchers speculated on the use of sub-millimetre waves for seeing through fog or haze with reduced scattering losses, locating objects hidden in camouflage, and detecting defects in optically opaque materials, in addition to other research areas such as high bandwidth communications and metrology. More recently, this list of promising applications has grown to include package inspection, quality control, non-destructive testing, and spectroscopic characterization of materials [1]. Many of these ideas exploit the unique properties of terahertz radiation which include the transparency of common packaging materials such as cardboard and plastics, the sub-millimetre wavelength which permits imaging with a diffraction-limited resolution similar to that of the human eye, and the fact that many interesting materials exhibit unique spectral fingerprints in the terahertz range which can be used for identification and chemical analysis.

In the 1960s and early 1970s, the challenges facing the field were also evident: a lack of suitable sources, sensitive detectors, and other components for the manipulation of radiation in this wavelength range. The most intense source of terahertz radiation was the HCN laser operating at 1.12 THz, first reported [3] only a few years after the development of the laser itself. The far-infrared FTIR spectrometer was also becoming a more common tool, with the advent of fast digital methods for computing Fourier transforms. Detection methods included pyroelectric detectors, hot electron bolometers, and several types of diode detectors.

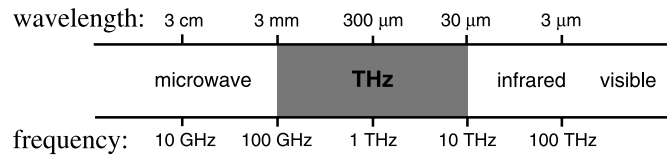


Figure 1. The terahertz region of the spectrum lies between microwaves and infrared, and is characterized by a free-space wavelength between $30\ \mu\text{m}$ and $3\ \text{mm}$. The photon energy corresponding to $k_{\text{B}}T$ at room temperature, $40\ \text{meV}$, is equivalent to a frequency of about $10\ \text{THz}$.

In addition to the many instrumentation challenges, the community also recognized that the opacity of the atmosphere, due to water vapour absorption, would inevitably place severe restrictions on the long-range transport of THz beams. Interestingly, Gebbie described free-space communications as the most easily imagined future application for sub-millimetre waves, while acknowledging the great challenges posed by atmospheric attenuation. He speculated that applications requiring short-range propagation would probably have greater impact [4]. In hindsight, this observation was correct; nearly all of the applications under current consideration involve relatively short-range interactions, with propagation lengths on the order of metres to tens of metres, or less.

The development of the far-infrared gas laser and the Schottky diode harmonic mixer inspired the first work in terahertz imaging in the mid-1970s by Hartwick *et al* [5]. Shortly thereafter, Cheo used a similar system for the detection of air bubble defects in the polyethylene insulation on high-power electrical cables [6]. This technology, although suitable for laboratory demonstration, was too complicated and specialized to inspire much further effort in imaging research.

At roughly the same time, the advent of high-power laser sources was opening up new possibilities for terahertz systems. In the early 1970s, several groups were able to generate bright tunable far-infrared radiation using the technique of difference-frequency generation in non-linear crystals, a second-order non-linear optical mixing process [7, 8]. Even at this early stage, these optically generated THz sources were already substantially brighter (per unit solid angle) than a $5000\ \text{K}$ blackbody source. This work ultimately served as the inspiration for the development of terahertz time-domain spectroscopy (THz-TDS), in which sub-picosecond optical pulses are used to generate broadband terahertz radiation, also via a second-order non-linear optical process [9–13]. In this system, a short optical pulse is used to both generate and detect terahertz radiation, via non-linear optical interactions between the optical pulse and a medium, typically a semiconductor. Hu and Nuss reported the first images acquired using THz-TDS (along with coining the term ‘T-rays’) in 1995 [14, 15]. These initial images (see figure 2) have inspired a great deal of excitement and much of the subsequent development of terahertz imaging systems and techniques. The annual number of journal articles on the subject of terahertz imaging, only about 8 in 1996, grew to over 80 by 2005. The 1995 paper by Hu and Nuss has been referenced well over 200 times.

The recent history of the field has been one of rapid expansion, with the development of both new imaging techniques and also new technologies for terahertz sensing [16]. The low temporal coherence of terahertz pulses has been exploited in time-of-flight imaging [17], and more recently in a variety of different tomographic and synthetic aperture imaging configurations [18–24]. Of particular note is the pioneering work of Zhang and co-workers, who have used large-area electro-optic sensors to demonstrate video-rate terahertz imaging over a $\sim\text{cm}^2$ focal plane area [25, 26]. This group has also developed a chirped-pulse technique for measuring an entire THz waveform along a line (1D imaging) using a single shot [27–29].

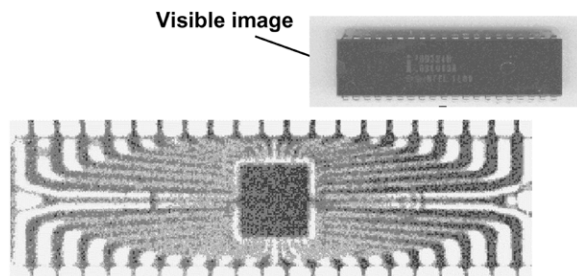


Figure 2. One of the first images acquired using a THz time-domain system. This shows a transmission image of a semiconductor integrated circuit, through the black epoxy package which is transparent to terahertz radiation. The metallization inside the package is clearly visible, as is the semiconductor wafer in the centre. The spatial resolution of this image is roughly $250\ \mu\text{m}$. The inset shows an optical image of the sample. Adapted from reference [14].

The implementation of near-field techniques for sub-wavelength resolution has been actively pursued using a variety of methods [30–38]. Some imaging results have also been reported using continuous-wave (cw) THz radiation [39–46], spurred in large part by developments in cw THz sources such as the recent invention of terahertz quantum cascade lasers [47, 48] and the development of terahertz parametric oscillators [49]. Finally, there have been numerous reports of specific applications of terahertz imaging to a variety of problems ranging from quality control [50] to detection of illegal drugs [39, 51]. In this review, we will describe each of these advances in some detail, and also discuss some of the advantages and limitations of THz imaging with respect to many of the proposed industrial and commercial uses.

2. Diffraction-limited imaging with terahertz radiation

Over the last 10 years, the majority of research developments in terahertz imaging have made use of terahertz time-domain spectroscopy, in which the terahertz radiation is generated in the form of single-cycle pulses of duration 1 ps or less (see figure 3). This progress has occurred in parallel with numerous dramatic advances in state-of-the-art sources and detectors for continuous-wave (cw) terahertz radiation. Many of the proposed applications for terahertz imaging, including several that have previously been studied using time-domain methods, are clearly better suited for a frequency-domain approach. Indeed, each proposed application for terahertz imaging will have its own unique optimal system configuration (e.g. pulsed versus continuous, broadband versus narrowband, spectral resolution versus temporal resolution, etc). In many cases, this optimal configuration has not yet been determined.

In this review, we describe imaging results that employ both time-domain systems and other terahertz sources. Since the preponderance of research has exploited time-domain methods, we first discuss the unique aspects of these short-pulse terahertz spectrometers, and the conventional operation of a time-domain imaging system. However, where relevant we will also discuss (or at least provide references to) frequency-domain imaging configurations. It must be pointed out that this review is not intended to contain a detailed discussion of the operation parameters of any of the terahertz systems that have been used for imaging, nor is it intended to serve as a guide for the construction of such systems. Clearly, this rapid technological progress has inspired many new avenues for spectroscopic research, which have been reviewed recently [52] and which will not be discussed here. It is also useful to distinguish the present discussion from considerations of millimetre-wave imaging [53, 54] or infrared arrays [55]. Instead, we focus specifically on the issues pertinent to imaging with terahertz

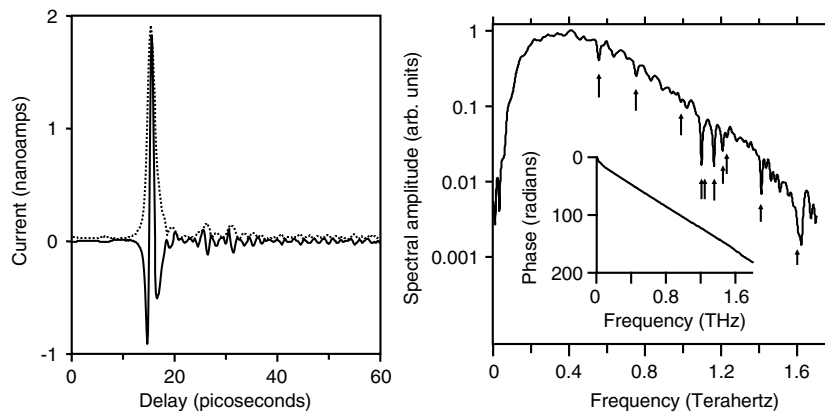


Figure 3. (left) A typical time-domain terahertz waveform, measured in ambient air. The oscillatory features which follow the initial single-cycle transient are the result of water vapour in the beam path. The dotted curve shows the intensity envelope, computed from the measured electric field $E(t)$ using a Hilbert transform. (right) The spectral amplitude $|E(\omega)|$ derived from the field shown at left by Fourier transform, on a log scale. The vertical arrows indicate the spectral positions of tabulated water vapour absorption lines. The inset shows the spectral phase, also derived from the time-domain measurement. This is essentially linear, as expected for a single-cycle pulse. The effects of the water vapour absorption lines on the phase are measurable [67], but are too small to see in this display.

radiation. References are provided for the interested reader who wishes to learn more about the detailed operation of any of the terahertz systems mentioned here.

2.1. Advantages and disadvantages of the time-domain approach

The performance characteristics of a THz-TDS system has been reviewed in several previous publications [1,56–58], and will not be discussed in great detail here. We will provide a very brief description of the spectroscopic technique, and then focus on the numerous features of this spectrometer which have proven advantageous for imaging.

A THz-TDS system starts with a femtosecond laser, producing a train of pulses of typically ~ 100 fs duration, at a repetition rate which is usually near 100 MHz. We split this pulse train into two using a beam splitter. One half is used to generate the terahertz radiation, while the second half is used to gate a detector. Ideally the detector is sensitive to the incoming terahertz field only for a brief period of less than one picosecond. We can use this brief temporal window to sample the terahertz field at various delays, relative to the arrival of the terahertz pulse at the detection point. In other words, we determine the terahertz electric field as a function of time by measuring the value of $E_{\text{THz}}(t)$ at a particular value of t , and then repeat the measurement many times, at many other values of t . To make these repeated measurements, we use many identical copies of the THz electric field. We expect that all of the pulses in this pulse train are identical to each other. In that way, when we measure E_{THz} at a time $t = t_1$ for one pulse in the train, and then move the delay line to measure E_{THz} at a time $t = t_2$ for a different pulse in the train (and so on), we can connect these multiple independent measurements and say that we have measured ‘the shape of the terahertz pulse’. Of course, in most cases we use many consecutive pulses in the train to obtain each measurement at each delay time t_j , in order to take advantage of the noise reduction by signal averaging. So, we are not really measuring the shape of a single pulse, but rather the average shape of many THz pulses, all of which are

(ideally) identical to each other. Sampling techniques of this sort, which rely critically on the precise synchronization between the terahertz field and the pulse used to gate the detector, are widely used in ultrafast optics and optoelectronics.

Clearly, optical sampling only works if every THz pulse in the pulse train is identical. If the shape of the THz pulse is evolving on a time scale comparable to (or shorter than) the measurement time, it is not possible to sample the waveform accurately. In addition to this fundamental issue, there are some other disadvantages to optical sampling. Like any sampling technique, it takes time to obtain the data. In principle, the acquisition time cannot be less than $N \cdot \delta t$, where N is the number of measured values of the electric field required in order to characterize the terahertz pulse, and δt is the pulse-to-pulse spacing of the pulse train. Because we usually take advantage of signal averaging, the acquisition time is usually *much* longer than this minimum value. Another problem inherent to sampling measurements is that they require a method for varying the delay of the sampling gate (i.e. the probe pulse) relative to the terahertz pulse. This is most often accomplished using a mechanical delay line, moving a mirror to vary an optical path length.

There are two common methods used to generate terahertz radiation with femtosecond optical pulses, both of which provide the high degree of synchronization and repeatability required for detection using optical sampling. Photoconductive techniques make use of a resonant excitation of a semiconductor by a femtosecond laser, generating currents through the excitation of electrons and holes [11, 59]. This rapid change in the current generates a burst of THz radiation according to Maxwell's equations, since $E_{\text{radiated}}(t) \sim (\partial J / \partial t)$. To optimize the process, a metal pattern is typically applied to the semiconductor surface, in the form of an antenna structure. With this metallization, one can apply a large dc bias to the illuminated region of the semiconductor, which enhances the generated photocurrent. The antenna structure also helps to couple the THz radiation into free space. In contrast to this resonant absorption process, the electro-optic method is a non-resonant process, relying on the 2nd-order susceptibility of non-centrosymmetric media such as inorganic crystals [60, 61]. In this case, known as optical rectification, one can describe the generation process as a difference mixing between all possible pairs of spectral components within the bandwidth of the femtosecond optical pulse. All of these difference-frequency components add coherently to produce a short burst of THz radiation [62, 63].

For the detection of free-space THz pulses, there are also two commonly employed methods. In the case of photoconductive sampling, one again uses an above-band-gap (resonant) excitation in a semiconductor. During the short sampling window, the THz pulse induces a short burst of photocurrent. Although this short current pulse is too fast to resolve using conventional electronics, the average current (averaged over many identical pulses) can easily be measured as a function of the delay between the optical gate pulse and the THz pulse. In this case, the width of the optical sampling window is determined by the charge carrier recombination or trapping lifetime in the semiconductor. Typically, fast photoconductors such as radiation-damaged silicon or low-temperature-grown GaAs are used, to provide sub-picosecond sampling resolution. The second method is based on free-space electro-optic sampling, in which the THz field induces a birefringence in an electro-optic medium. This birefringence is sampled by an optical probe beam, as a function of the delay between the probe and THz pulses [64–66]. Here, the sampling resolution is determined largely by the duration of the optical probe pulse.

The terminology 'terahertz time-domain spectroscopy' is generally applied to any spectrometer which makes use of any combination of the aforementioned generation and detection mechanisms, and which therefore relies on the precise synchronization between the femtosecond optical pulse and the terahertz pulse. It is important to note that, in either case, optical sampling provides a direct measurement of the terahertz electric field $E(t)$, not merely

the intensity $I(t)$. The measurement is sensitive only to coherent radiation, and moreover only to radiation which is phase-locked to the repetition rate of the femtosecond oscillator. As a result, both photoconductive and electro-optic sampling are blind to thermal radiation, and therefore the detection operates at room temperature without significant degradation of performance. This eliminates the requirement for liquid cryogenics which had previously limited the broader use of THz spectrometers.

Other useful aspects of the time-domain spectrometer are illustrated by figure 3, which shows a typical waveform and the corresponding spectral amplitude and phase. The left panel shows the raw data from a photoconductive sampling measurement, which is the average photo-induced current in a terahertz substrate antenna as a function of the delay between the terahertz pulse and the optical gate pulse. This is approximately proportional to the terahertz electric field $E(t)$, which contains both amplitude and phase (i.e. timing) information. Here, it is clear that optical sampling permits one to distinguish between positive and negative electric fields, and also to determine the time (relative to an arbitrary reference $t = 0$) at which the terahertz pulse arrives at the detector.

In order to obtain the temporal intensity $I(t)$, one requires both $E(t)$ and its complex conjugate, since $I(t) \propto |E(t)|^2 = E(t)E^*(t)$. This is most easily obtained from the (real-valued) measurement of $E(t)$ by the Hilbert transform, conventionally used in signal processing to obtain the complex envelope of a real-valued signal. The Hilbert transform is obtained by convolving $E(t)$ with $1/\pi t$. In the frequency domain, this is equivalent to shifting the phase of the negative frequency components by $+\pi/2$, and of the positive frequency components by $-\pi/2$. The dotted line in figure 3 shows the intensity $I(t)$ obtained from $E(t)$ in this fashion. A typical (not time-resolved) power-law detector (like a bolometer) would only measure the average value of $I(t)$, which contains no information about the phase of the field. In this example, the duration of $I(t)$ (as measured by its full-width at half-maximum) is about 1.6 ps.

On the right side of figure 3, the amplitude and phase of the Fourier transform of $E(t)$ are displayed. The amplitude spectrum $|E(\omega)|$ is quite broad, extending over more than an order of magnitude in wavelength, from below ~ 100 GHz to beyond 1.5 THz. It also contains numerous sharp dips, at the locations of tabulated rotational transitions of water vapour [67] (as indicated by arrows). The spectral phase $\phi(\omega)$ shown in the inset, has been unwrapped to remove 2π phase jumps, and is nearly linear with frequency as expected for a single-cycle pulse. Phase-sensitive measurements are customary in microwave systems but quite unusual for optics. The additional information contained in the phase can be extremely useful in image formation, since it correlates with the thickness, and in many cases the density, of a sample under study.

Another unique characteristic of THz-TDS is the broad bandwidth of the radiation, broader than any other source (excluding thermal sources) in the terahertz range. Typically, the bandwidth can span more than an order of magnitude in wavelength. Broadband coverage is valuable for spectroscopic measurements, which can be used to identify the chemical composition of unknown materials in an image or to locate materials according to their terahertz absorption signatures. This capability is nicely illustrated in figure 4. Here, a pipe was inserted into a block of polystyrene foam (which is nearly invisible to THz radiation [68]). A polar gas, CH_3F , was pumped into the pipe, and allowed to slowly diffuse through the foam block. Images of the block can be formed using the spectral information at the particular frequencies where this molecule absorbs THz radiation. A series of images at successive times show how the vapour diffuses away from the end of the gas pipe [69].

The broad bandwidth also implies a short coherence length, which has a number of benefits. The coherence length defines the spatial resolution along the propagation direction (also known as the range resolution), as has been demonstrated in tomographic and time-of-flight imaging

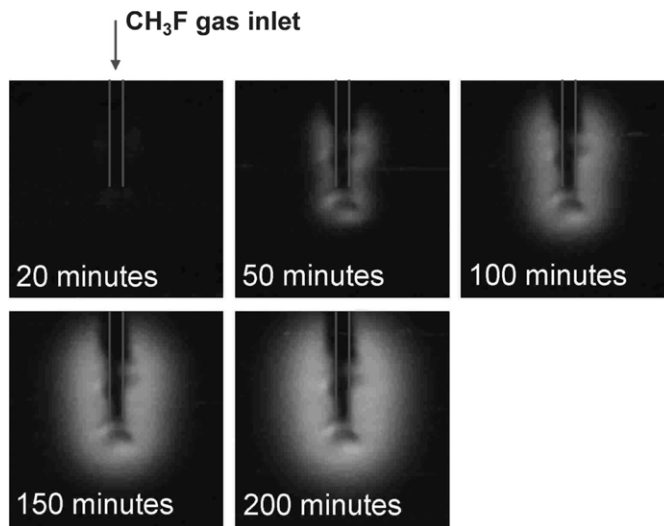


Figure 4. A series of images of a block of polystyrene foam with a gas pipe inserted into one side. A polar gas is pumped into the pipe and diffuses through the foam block away from the end of the pipe. THz images obtained with a broadband system capture the spectroscopic signature of the gas, and can be used to image the spatial distribution at various times after the gas injection. Adapted from [69].

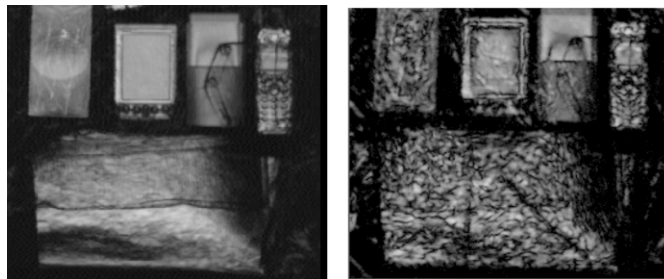


Figure 5. (left) An image of a series of articles, measured through a layer of clothing which gives rise to random scattering of some portion of the transmitted terahertz beam. This image was composed by integrating the spectral content of the time-domain waveform (between 200 GHz and 1 THz) at each pixel. (right) Processing the same image using only a narrow portion of the spectrum (430 ± 3 GHz) gives rise to image speckle which results from the interference between many different randomly scattered wavelets. Speckle is suppressed in the broadband image because the coherence length is much smaller, so wavelets which travel paths of different length cannot interfere with one another. Images courtesy of David Zimdars, Picometrix, Inc.

configurations (discussed below). A short coherence length also suppresses speckle, which arises from the interference of many randomly scattered wavelets at a rough surface or interface. Speckle can only arise if the path length differences between any pair of scattered wavelets is smaller than the coherence length of the incident radiation. This is strongly suppressed in the case of pulsed THz systems [70], as illustrated in figure 5. Here, a series of articles are imaged through a layer of clothing using a broadband TDS system. When the full bandwidth of the spectrometer is used to create the image, the clutter from scattering off of the clothing layer is suppressed, resulting in a superior image quality.

It is also worth noting some of the limitations of working with THz-TDS systems. A primary challenge is the power in the THz beam, which is quite low (typically less than $1\ \mu\text{W}$ average power) because of the inefficiency of non-linear optical conversion. One can argue that average power is not the most useful performance metric for a system employing coherent detection. A more useful metric is the dynamic range, which can be quite high in THz-TDS, even though the THz power is low [71]. This is a result of the coherent detection which effectively rejects many common sources of noise. This high dynamic range permits measurements even in situations where only a tiny fraction of the generated radiation reaches the detector. Examples include studies of random multiple scattering [72,73], and even the imaging of objects buried in random scattering powders [74]. Nevertheless, it is important to note that existing commercially available focal plane detectors (such as, for example, pyroelectric cameras) require much more power to operate than the THz-TDS systems generally produce (e.g. a minimum power level of $100\ \mu\text{W}$ per illuminated pixel). As a result, the majority of time-domain imaging systems rely on raster scanning of either the THz beam or the object, so that images can be assembled serially using a single detector or perhaps a few operating in parallel. This places a significant limitation on the image acquisition rate. Concerns about power may also play a role in experiments which require long distance atmospheric propagation or which seek to study material non-linearities at terahertz frequencies.

Other difficulties are inherent in the nature of the time-domain system. For instance, the time-domain scanning puts a practical upper limit on the spectral resolution which can be achieved. The spectral resolution δf is given by the inverse of the duration of the temporal scan, which in most cases is limited by the length of a scanning delay line as in a conventional Fourier transform spectrometer. With 15 cm of travel, a typical mechanical delay line will provide up to 1 ns of delay range, corresponding to $\delta f = 1\ \text{GHz}$. This value is inadequate for high-resolution gas-phase spectroscopy, since Doppler-broadened linewidths of THz transitions are typically in the MHz range [1], although it is often adequate for identification of unknown gases [75]. Also, experiments which require radiation in the higher frequency range may require a source other than THz-TDS. The high dynamic range typically quoted for THz-TDS measurements is a frequency-dependent quantity, which decreases exponentially with increasing frequency as shown in figure 3 [71]. Thus, a THz-TDS system may compare very favorably to an electronic cw system based on a Gunn diode operating below 1 THz, for example [70], but would perform less well in comparison to a quantum cascade laser operating at 4.9 THz [45]. Finally, one practical disadvantage is the requirement for a femtosecond optical source. Recent dramatic advances in femtosecond fiber laser technology are beginning to overcome this problem, but the laser is still the most expensive and sophisticated piece of equipment in the spectrometer. Recently, considerable effort has been directed towards the goal of developing a compact and inexpensive terahertz imaging system [76–79].

2.2. *Imaging with a time-domain spectrometer*

The first TDS imaging system, reported in 1995, implemented an operational method which has subsequently been replicated many times [14, 15]. A typical system diagram is shown in figure 6. This shows a time-domain spectrometer based on photoconductive antennas—electro-optic generation and detection are also commonly used [80, 81]. In order to be suitable for image formation, a second set of focusing optics are inserted into the THz beam to form an intermediate focal spot halfway between the THz transmitter and THz detector.

For image acquisition, one of the key considerations is the rate at which THz waveforms can be acquired, since this often determines the time for forming an image. Typically, a motorized scanning stage is used to raster the object to be imaged through the terahertz beam

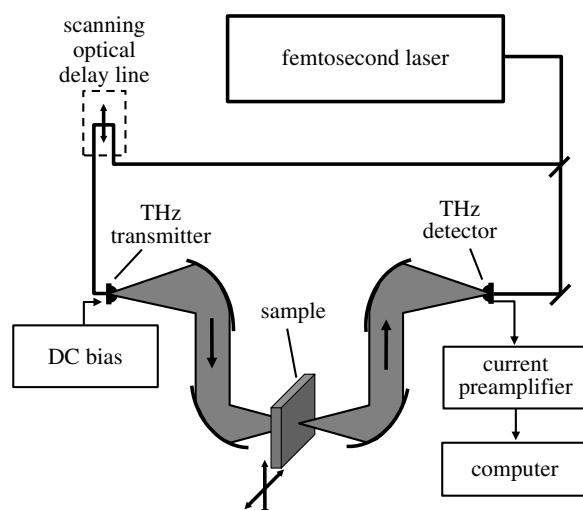


Figure 6. A schematic of a typical transmission-mode raster-scan time-domain imaging system.

focus, so that image data is acquired one pixel at a time. In the earliest example, THz waveforms were measured at a rate of 20 waveforms per second, so acquiring a 100×100 pixel image took close to 10 min. This rate was determined by the scan rate of the optical delay line, a galvanometric scanner with a corner cube mirror. Modern THz imaging systems which use this raster-scanning method employ more sophisticated methods for generating optical delay, and thus can run at substantially higher speeds. In such systems, however, there is frequently a trade-off between the scan range (as measured in picoseconds) and the scan rate (number of waveforms per second). The highest scan rates (e.g. thousands of waveforms per second) can be achieved using a piezo-electric device, but with a limited (tens of picosecond) scan range. At these higher rates, the image acquisition time may no longer be limited by the time to measure a THz waveform, but instead by the rate at which the object (or the THz beam) can be raster scanned. However, the more limited scan range does limit the information contained in each waveform. As noted above, a shorter scan range limits the spectral resolution of the measurement. A shorter scan range also limits the range of depths to which the THz pulse can penetrate through a material and still be detected, since a larger optical depth could delay the pulse outside of the temporal window of the measurement. This latter effect will be illustrated more clearly in the discussion of time-of-flight imaging (see below). Other types of mechanical scanning devices (e.g. spinning mirror devices) can generate several hundreds of picoseconds of delay range with a scan rate in the vicinity of 100 Hz [82]. In any event, the motion of the scanning delay line must be synchronized to the raster scan of the object, so that it is possible to determine the location of the object at the moment each waveform is acquired.

Recently, several groups have demonstrated that it is possible to dispense with the mechanical scanning delay line entirely, and instead make use of asynchronous optical sampling [83, 84]. In this approach, two femtosecond lasers are used instead of one. The repetition rate of one laser is locked to that of the other, with a fixed frequency offset. One laser is used to generate the THz pulse, and the second to gate the detector. In this way, the delay of the THz pulse sweeps automatically, relative to the gating of the detector, at a rate which is determined by the frequency offset between the two lasers. This eliminates the moving parts, at the expense of a second laser and feedback electronics. This

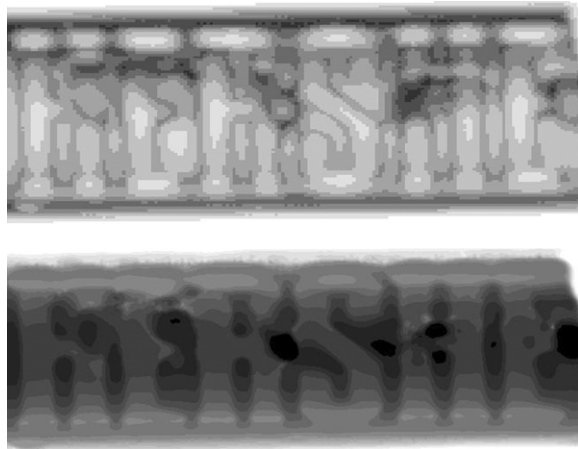


Figure 7. Terahertz transmission images of a chocolate bar. The upper image is assembled using the peak-to-peak amplitude of the transmitted time-domain pulse. Here, the embossed lettering is only visible because of scattering effects at the stepped edges, whereas the almonds embedded in the chocolate are clearly visible due to their larger absorption coefficient. The lower image shows the variation in transit time of the THz pulse through the sample. In this case, the almonds are much less evident, but the thickness variations associated with the embossed letters on the sample surface are quite clear. Adapted from [75].

approach has not yet been used for imaging, but has proven effective for THz spectroscopic measurements [85].

Once the data are acquired, the next task is the formation of an image. A full data set consists of a complete THz time-domain waveform (see figure 3) corresponding to each pixel of the image. These waveforms obviously contain a great deal of information: the amplitude and phase of the transmitted terahertz pulse, for many spectral components. A two-dimensional false-color image can be formed using any subset of this large data set. Typically, images formed using different portions of the data contain different types of information about the sample. Figure 7 illustrates this point, showing two THz images of a chocolate bar [75]. In the upper image, the grey-scale is determined by the peak-to-peak amplitude of the time-domain THz pulse at each pixel. The chocolate does not absorb much THz radiation, but several other features are visible. First, the sample has a plano-convex cross-sectional profile, and is therefore thinner at the top and bottom than in the middle. Second, the embossed letters are visible only because of scattering effects at their stepped edges, and as a result are rather difficult to read. Finally, because almonds absorb more THz radiation than chocolate, they can be easily detected using this technique. The lower image shows the same data set, except that this image is formed using the transit time of the THz pulse through the sample, rather than the amplitude. Here, the image primarily contains information about the thickness of the sample at each point, since a thicker sample delays the THz pulse by a greater amount. As a result, the embossed lettering and the overall thickness variation are much more prominent. The almonds are nearly invisible, except for the black regions where the transmitted pulse was too small for an accurate determination of the arrival time.

Images such as this one, in which the time delay or phase of the pulse is used to encode the data, can often be more valuable than images which depict the amplitude transmission. Indeed, the spectral phase of the THz pulse can be determined with far greater accuracy than the amplitude [86]. The primary source of noise in a THz-TDS system is the amplitude and

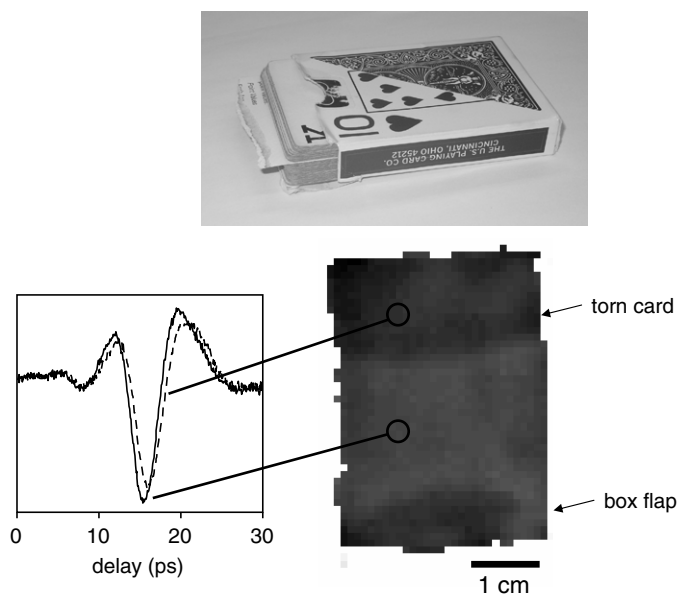


Figure 8. A terahertz transmission image of a deck of cards. The photograph shows a single card, which has been torn in half, sticking out of the deck. For the terahertz image, this card was inserted into the deck. The THz image is encoded with a grey scale showing the phase of the transmitted pulse at a frequency of 200 GHz. The upper (darker) portion of the image corresponds to a slightly larger phase, resulting from the additional thickness of the torn card. The lower dark portion is also somewhat thicker because of the flap of the box in which the cards are held. The two waveforms illustrate the typical results at the two locations indicated by the black circles. The extra delay of the dashed waveform (roughly 0.6 ps) is evident in these waveforms, which were acquired with no signal averaging (i.e. a single sweep of the scanning delay line at each pixel).

pointing instability of the femtosecond laser source. These noise sources are manifested as amplitude fluctuations in the peak-to-peak THz pulse amplitude, but have little effect on the path length delay (which is equivalent to the phase of the THz pulse). Experimentally, a pulse-to-pulse timing jitter of less than 10 femtoseconds (0.02π radians at 1 THz) can readily be achieved, even with no special effort to stabilize the optical components [15]. This can be compared with peak-to-peak amplitude fluctuations, which are typically on the order of a few per cent for a TDS system which uses a mode-locked Ti:sapphire laser. This excellent sensitivity is illustrated by figure 8, which shows a terahertz transmission image of a deck of cards. One card in the deck has been torn into two pieces and one piece inserted back into the deck. This torn card is clearly visible in the image, which is encoded according to the phase of the terahertz pulse at a particular frequency, at each pixel. In the upper part of the THz image, where the thickness of the deck is one card larger, the transit time is slightly longer (by about 0.6 ps).

Owing to the broadband nature of the radiation, the diffraction-limited focal spot in the centre of the THz beam path can have a rather complicated character, which can depend on the detailed design of the optical system. For example, it is common to find that the focal spot diameter is strongly frequency-dependent. In this case, care must be exercised in defining the spatial resolution of an image. This effect is illustrated in figure 9, which shows a series of terahertz images of a circular hole in a metal foil. These images are all derived from a single data set, consisting of a collection of 3721 THz waveforms, one for each pixel. To form each

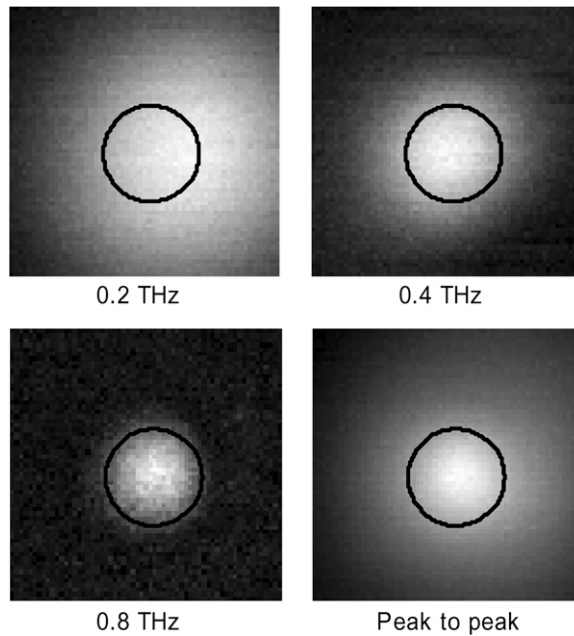


Figure 9. Terahertz images of a small circular hole in a thin metal plate. The black circle in each image shows the location and size of the 2.18 mm diameter hole. The field of view in each image is $6\text{ mm} \times 6\text{ mm}$. The first three panels show images formed by selecting a particular frequency component and plotting its amplitude at each pixel. The fourth (lower right) panel shows the peak-to-peak amplitude of the time-domain waveform at each pixel. The resolution in this case is similar to that achieved using the frequency component with the largest amplitude, which in this example is roughly 0.3 THz.

image, these waveforms are converted to the Fourier domain by numerical Fourier transform. By selecting a specific frequency within the THz bandwidth, one can select the spot size of the THz beam, which varies in proportion to the wavelength. Thus, images formed using a high-frequency component show less blurring because the spot size of the THz beam at that frequency is smaller, while images formed using a low-frequency component are blurrier. The final image (lower right panel of figure 9) shows the result of using the peak-to-peak amplitude of the time-domain waveform, rather than a specific spectral component. This amplitude parameter depends on all of the frequency components, not just one, so the resolution is intermediate between the low-frequency and high-frequency cases.

Although the use of polarization techniques has not yet become widespread in the terahertz community, this promising area is worth a brief comment. The terahertz beam generated by a typical photoconductive antenna is linearly polarized, with a typical polarization ratio of better than 10:1 for a conventional lens-coupled dipole antenna [87, 88]. Electro-optic generation of THz pulses produces even higher polarization purity, and one can easily achieve extremely purely polarized THz beams using a broadband wire grid polarizer. On the other hand, control of the polarization can be quite challenging for anything other than pure linear polarization, because commercially available optical components such as wave plates are not useful over a full octave of spectral bandwidth [89, 90]. However, even linear polarization can provide a useful contrast mechanism in imaging [91]. For example, figure 10 shows terahertz transmission images of a plastic coin, illuminated with linearly polarized radiation. The image obtained from the component parallel to the incident field (a) shows a decreased amplitude at

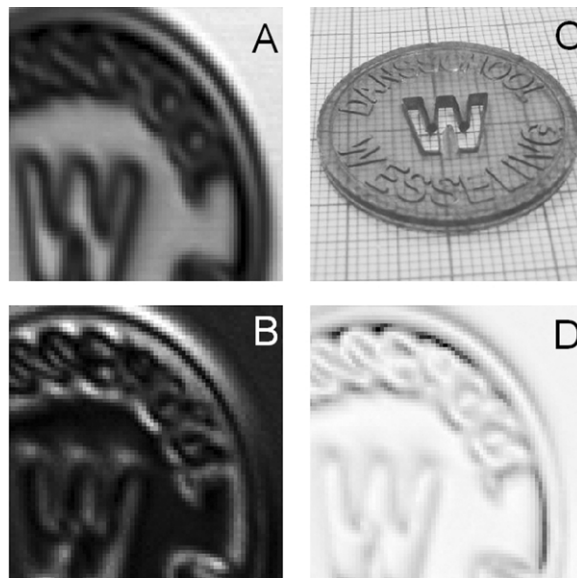


Figure 10. Transmission images of a plastic coin illuminated with a linearly polarized terahertz beam. Panel A shows the transmitted terahertz power parallel to the incident polarization, while panel B shows the power measured in the perpendicular configuration. Panel C shows a photograph of the object. Panel D shows the angle of polarization rotation, computed from A and B. Rotation angles as large as 45° are observed. Adapted from [91].

the edges of the coin, while the image obtained with the perpendicular component (*b*) shows enhanced signal at the edges. This indicates a rotation of the polarization due to scattering at the edges of the sample. The image in (*d*) shows the degree of polarization rotation, defined as $\arctan(E_{\perp}/E_{\parallel})$. The measurement of the perpendicular component allows one to distinguish between scattering and absorption in an image. Polarization information was also used to image carrier density inhomogeneities in doped semiconductor films, via the terahertz Hall effect [92].

Another method for discriminating scattered radiation from reflections is dark-field imaging. In this technique, a large collection aperture is used to gather radiation returning from a sample's surface. A beam stop is used to block the direct back-reflection, so that only obliquely scattered or diffracted radiation is measured. This technique enhances the contrast for edges, and can be used to distinguish between scattering and absorption, for example. Dark-field imaging, well-known in the realm of optical microscopy, has recently been used to study biological samples with terahertz radiation [93].

2.3. Time-of-flight imaging

Although many common materials are transparent in the THz range, certain substances such as metals are opaque, and highly reflective. Living tissue is also opaque, due to the high liquid water content, and therefore also cannot be imaged in transmission. Terahertz imaging of materials such as these requires a reflection imaging geometry. The broad bandwidth of the THz radiation is an additional advantage in a reflection mode, since it permits one to obtain depth information and therefore construct a full three-dimensional representation of an object.

The first demonstration of three-dimensional terahertz imaging was described in 1997 [17]. This system was essentially equivalent to the one shown in figure 6, except that the optical

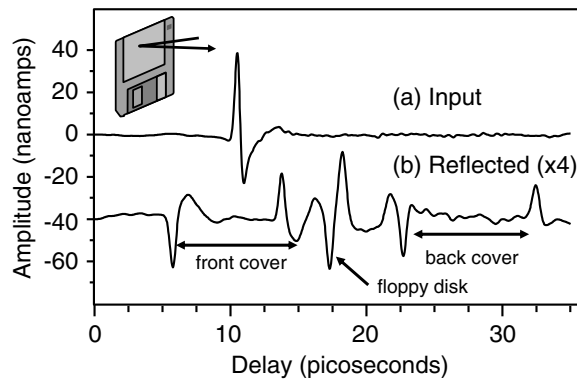


Figure 11. Terahertz pulses measured in a reflection geometry. (a) the input pulse, measured with a mirror at the confocal reflection location (i.e. the position of the sample). (b) a terahertz pulse reflected off of a conventional 3.5" floppy disk. Multiple reflections can be seen, one from each dielectric interface in the sample. Lower curve is vertically offset for clarity. Adapted from [17].

setup was folded at the location of the sample so that the THz beam reflected off of the sample rather than transmitting through it. One can best understand the nature of the signals measured in this configuration by studying a particular example. In this case, the object in question is a conventional 3.5" floppy disk, a sample which consists of a series of smooth dielectric layers (the front and back plastic covers, and the thin plastic disk which contains the data). This set of layers presents a series of step discontinuities in the dielectric (air-to-plastic, plastic-to-air). When illuminated by a single-cycle THz pulse at normal incidence, each step generates a reflected THz pulse. Since each interface is located at a different distance from the receiver, each of these reflections arrives at the receiver at a unique time delay. The signal measured in reflection, therefore, consists of a train of THz pulses, as shown in figure 11. The amplitude of each pulse in the train provides information about the magnitude of the dielectric change across the interface from which it originated. The time delay between successive pulses in the train provides information about the thickness of the intervening layer. In fact, from measurements of this type on samples with smooth parallel transparent layers, it is possible to obtain the spatial variation of the refractive-index profile along the direction of propagation of the THz beam.

Figure 12 shows a pair of images collected using this reflection geometry. The upper image shows a conventional THz image, displaying the total reflected THz energy as a function of the position of the object (in the two dimensions perpendicular to the beam propagation direction). The metal hub is white in this image because it reflects essentially all of the THz radiation, whereas the dielectric surfaces (plastic, $n \sim 1.5$) reflect only a few per cent of the total energy. The lower image shows a single line scan along the dotted line in the upper image. In this image, the vertical axis is depth into the sample. All of the reflecting surfaces are clearly resolved. In addition, the sign of the reflected pulses can be used to provide additional information. A quick inspection of the lower waveform in figure 11 shows that the reflections from an air-to-plastic interface are negative-going, whereas a reflection from a plastic-to-air interface are positive-going. This follows directly from the sign of the Fresnel reflection coefficient, which changes when the sign of the index discontinuity changes. This information can be encoded in the image using false color, to show which surfaces correspond to 'air above' and which correspond to 'air below'. Because the metal hub is opaque, the image cannot contain any information about the region behind it. The faint surface which appears behind this metal

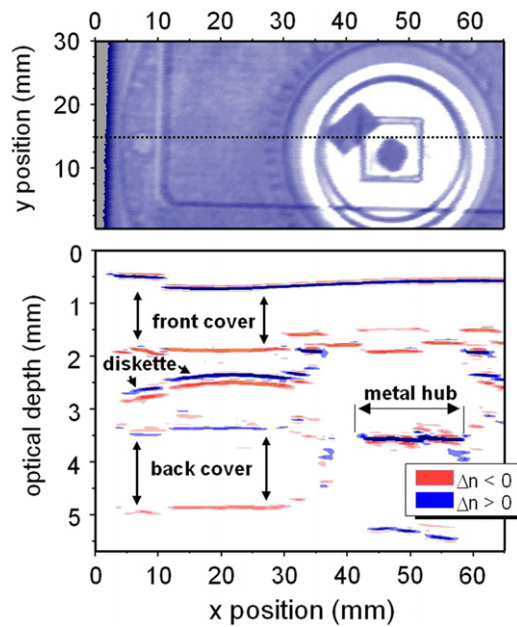


Figure 12. Images of a portion of the floppy disk, measured in a reflection configuration. The upper image shows the total terahertz power at each pixel, as a function of the two lateral dimensions. The lower image shows a time-of-flight slice along one row of the upper image (at the location of the dotted line). All of the internal (buried) interfaces can be clearly resolved. The metal hub, on the right side, is a strong reflector, and therefore gives rise to a multiple reflection which appears in the shadow region beneath it. Adapted from [17].

object is actually a multiple reflection between the metal hub and the inner surface of the front cover. Such ‘multiples’ are well known in acoustic imaging, and can be removed from images using numerical post-processing.

Although originally described as a tomographic measurement [17], this technique is more appropriately deemed time-of-flight imaging. This imaging mode is equivalent in many ways to an ultrasound B-scan. As with a B-scan, the length of the temporal data acquisition window determines an upper limit on the depth to which image data can be acquired. For the waveform in figure 11, a 30 ps window is sufficient to capture all six of the back-reflected pulses from the floppy disk. A thicker sample would, of course, require a longer window. This could be accomplished either by scanning continuously over a longer duration, or by acquiring several short scans and subsequently stitching them together in post-processing. One distinction between ultrasound measurements and THz imaging is the possibility for spectroscopic analysis which is offered by the specific interactions of THz radiation with certain materials [94–96]. However, because of the multiple discrete reflections that are present in a measurement of this sort, the simple relationship which defines the achievable spectral resolution of a TDS measurement is not applicable in these time-of-flight measurements. Sophisticated numerical deconvolution procedures would generally be required in order to extract spectroscopic data from a waveform which also contains multiple reflections.

A first step in this challenge is to simultaneously determine the reflectivity and the distance to a single reflecting surface. If the reflection coefficient is complex, then the phase changes associated with the reflectivity can be difficult to distinguish from the linear phase shift associated with a small displacement of the sample along the propagation direction. Ino *et al*

have investigated the use of a phase retrieval algorithm to separate out these two effects, and thereby obtain a measurement of the sample height profile which is independent of the reflection coefficient of the material [97].

Although it is conceptually simpler to consider in terms of a reflection geometry, time-of-flight imaging can also be implemented in a transmission mode. In this case, the number of reflections experienced by each measured pulse is even, rather than odd. Consider, for example, a pulse transmitting through a single slab of material. The ballistic (unscattered) pulse experiences zero reflections, while subsequent multiples experience two, four, etc, bounces inside the slab, as in a Fabry–Perot or etalon. This effect is more difficult to observe than the corresponding effect in a reflection measurement because each surface reflection weakens the pulse. For example, a single reflection off of an air-plastic interface is only about 20% of the amplitude of the incident pulse (i.e. $|E_{\text{refl}}/E_{\text{inc}}| \approx 0.2$). A doubly reflected pulse, therefore, is 20% smaller again, or only 4% of the amplitude of the incident field. This effect is therefore less useful in low index media, and is more often used with high dielectric media such as silicon, for which the reflection coefficient is closer to 50%. In this case, the effect can be useful for accurately determining the thickness of the dielectric layer in a transmission geometry [98, 99].

We also note that time-of-flight information (equivalent to phase contrast) can be obtained without the use of broadband pulses, as long as one can determine the phase of the radiation. As in the well-known technique of digital holography, two closely spaced single-frequency sources can also be used to obtain depth information, by comparing their phases. The advantages of this approach, including common-mode noise suppression and the elimination of a 2π phase ambiguity, have recently been described for terahertz radiation [100].

2.4. Depth resolution in time-of-flight imaging

In a time-of-flight imaging system, one of the important considerations is that of depth resolution. For two closely spaced reflecting interfaces, how close can they be before it is no longer possible to resolve them? The answer is illustrated by the lower curve in figure 11. The two central reflections, from the front and rear surfaces of the floppy disk, are nearly overlapped in time because these two surfaces are quite closely spaced (the floppy disk is quite thin). The ability to resolve these two closely spaced reflections is determined by the temporal duration of the THz pulses. If the pulses were shorter, then they could be closer together before overlapping. An equivalent formulation can be phrased in terms of the spectral bandwidth of the terahertz pulse. The resolution is given by half of the coherence length of the radiation, defined according to $L_C = c/\Delta\omega$, where $\Delta\omega$ is the spectral bandwidth and c is the speed of light in the intervening medium. The factor of 1/2 arises from the fact that the reflection from the further surface must travel through the intervening medium twice, once in each direction. In this example, the coherence length is about $200 \mu\text{m}$, just small enough to resolve the two surfaces of the thin recording medium. In the image shown in figure 12, the raw waveforms (e.g. figure 11(b)) were numerically processed to deconvolve the input pulse shape (figure 11(a)) prior to forming the image [17]. This is required in order to form an image in which these two closely spaced surfaces are distinct.

There are several different techniques which can be used to improve this depth resolution. One such technique relies on interferometry to improve the depth resolution, in a mode which is the time-domain analog of optical coherence tomography (OCT) [101, 102]. In OCT, an interferometer is used to temporally resolve a broadband light pulse by interfering it with a reference pulse, and thereby determine the time of flight in a reflection geometry. In THz-TDS, by contrast, an interferometer is not required to time-resolve the reflected waveform, because the detector already provides the necessary temporal resolution. Instead, we may use

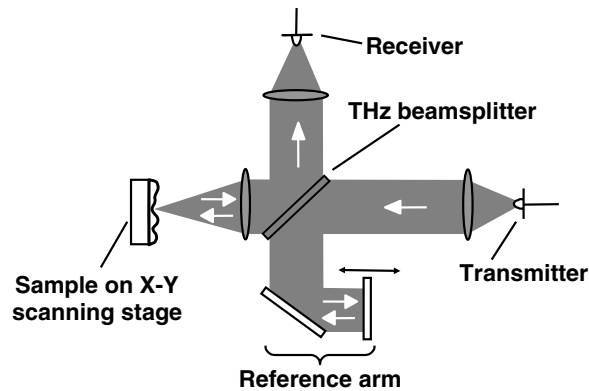


Figure 13. A schematic of a normal-incidence reflection imaging system, using a beam splitter to separate the incident and reflected beams. This beam splitter also directs a portion of the incident beam to a flat mirror on a manual delay stage, which can be used as a reference. The reflected pulse from the sample interferes with the reference pulse at the detector. Adapted from [102].

interferometric techniques to provide a background-free measurement for enhancing the depth resolution.

A schematic of the interferometer is shown in figure 13. The terahertz pulses are generated and detected using low-temperature-grown GaAs photoconductive antennas, gated with 50 fs laser pulses from a mode-locked Ti : sapphire laser. High-density polyethylene lenses are used to collimate, focus, and collect the THz beam, which is arranged in a Michelson configuration for reflection imaging. A high-resistivity silicon wafer is used as a beam splitter for the THz beam, dividing the pulse train into a sample and a reference arm. This wafer is 0.5 cm thick, so that multiple reflections within the beam splitter are delayed by over 150 ps relative to the initial THz pulse, and are not measured. A lens is placed in the sample arm of the interferometer, and the sample to be imaged is located at its focus. The beam in the second arm of the interferometer (the reference arm) is simply retro-reflected off of a flat mirror on a manual translation stage. The optical delays of the two arms are adjusted to be approximately equal.

In addition to providing lateral spatial resolution for imaging, the lens also provides the phase shift which permits background-free imaging. The pulse that passes through the lens acquires an additional phase (compared to the pulse that traverses the reference arm) as a result of the Gouy phase shift acquired by a focused Gaussian beam. This topological phase is a result of the variation in wave front curvature as the pulse passes through the focus, and is approximately equal to π [103]. Thus, when the pulses from the two arms of the interferometer reach the detector, they destructively interfere and a very small signal is measured. However, if the sample contains any feature that distorts either the amplitude or phase of the reflected THz pulse, this destructive interference is disrupted and a large signal is measured. In a sample containing multiple layers, the delay of the reference arm can be adjusted so as to cancel any one of the reflections from the sample, leaving the remaining interface reflections to be observed with reduced clutter. This destructive interference also provides a background-free method for waveform acquisition, which naturally eliminates common-mode noise arising from laser fluctuations or other external perturbations. Unlike an interferometer for visible light, a THz interferometer does not require sub-micron stability, and is thus far less sensitive to vibrations.

We have already pointed out the high degree of sensitivity to the optical phase provided by THz-TDS systems. The interferometer illustrated in figure 13 converts small phase shifts (small delay shifts) into changes in the THz amplitude, as follows. Consider one frequency

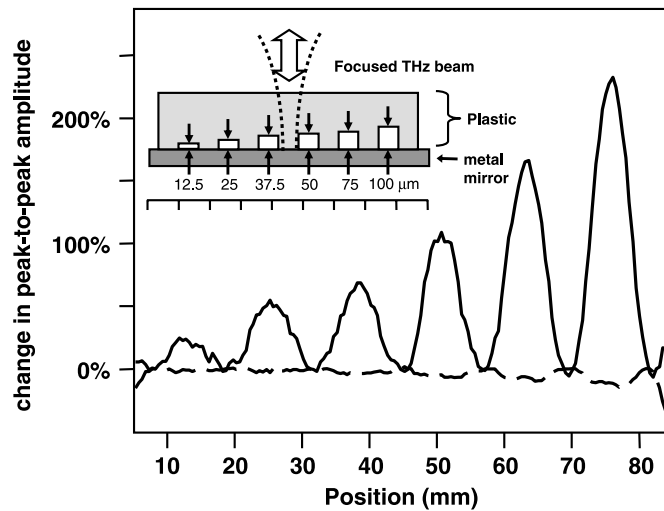


Figure 14. Line-scan reflection images across the model sample shown in the inset, which contains a series of air gaps between a block of plastic and a metal reflector. These line scans are normalized to the reflection from a portion of the sample without an air gap. Thus, this shows the fractional change in the terahertz reflection as a function of position across the sample. The two curves show the result with (solid) and without (dashed) the use of interferometry. The interferometric effect dramatically enhances the sensitivity to small (sub-coherence-length) features in the sample. Adapted from reference [102].

component of frequency ω in the reference arm of the interferometer, which can be described as $E_R = e^{i\omega t}$. The corresponding component of the sample arm waveform, with a π phase shift, may be written as $E_S = -e^{i\omega t} e^{i\phi}$. Here, $\phi = 2D\omega/c$ is the phase delay associated with the displacement of the reflecting surface in the sample arm, relative to zero optical path mismatch. We assume that D is much smaller than the confocal parameter of the focusing beam. The superposition of these two signals is $2i \sin(\phi/2) \cdot e^{i\omega t} e^{i\phi/2}$. In the limit of small displacement D , the amplitude of the interference signal is directly proportional to ϕ , and therefore to the displacement D . Thus, small changes in the phase of the sample arm wave lead to equivalent small changes in the amplitude of the interfered wave.

We demonstrate the ability to image below the coherence length limit using a Teflon–metal model, shown in the inset of figure 14. This model sample consists of a block of Teflon sandwiched on top of a metal mirror, with air gaps between the two pieces ranging from 12.5 to 100 μm in width. This sample is positioned so that the metal–plastic interface is located at the focus of the imaging lens in the sample arm, and adjusted so that, as it scans across the THz beam focus, the distance from the lens to this interface does not vary. Figure 14 shows two line scans cutting across this sample, through the series of air gaps, comparing the measured peak-to-peak amplitudes with and without the interferometric cancellation. This is displayed as a per cent change relative to the amplitude of a waveform measured at a position on the sample with no air gap. For these measurements, the delay of the reference arm has been used to optimize the cancellation of the pulse reflected from the metal–metal interface, at a point where there was no air gap in the beam. Clearly, with interferometry and destructive interference, the waveform amplitude increases when an air gap slides across the focal spot, whereas in the absence of interferometry, the waveform amplitude decreases due to the destructive interference between the two pulses reflected from the two interfaces in the sample. More importantly, the contrast of the interferometric signal is enhanced by more than

an order of magnitude over the non-interferometric signal. In the interferometric mode, the areas with no air gap show strong destructive interference. The change in the cancellation when an air gap is encountered results in a large increase in the amplitude of the measured waveform. As a result, it is possible to easily detect the smallest air gap using the interference effect. This 12.5 μm gap is roughly 25 times smaller than the coherence length of the terahertz pulses used to collect this data [101].

2.5. Tomography with terahertz radiation

Tomographic imaging is widely used in x-ray diagnostics, seismic prospecting, synthetic aperture radar, and ultrasonic imaging. Each imaging modality has its own source-detector configuration and image reconstruction algorithm, appropriate to the nature of the problem. For instance, in x-ray computed tomography (CT), the object can typically be viewed from any angle. As a result, the measured signal consists of a series of line integrals through the object under study, and can therefore be accurately described using a radon transformation (also known as a sinogram). To recover an image, a conventional inversion procedure such as the filtered back-projection algorithm is generally used [104, 105]. In contrast, seismic imaging of the earth's crust can only be performed from one side, in a reflection configuration, but unlike with x-rays, phase (i.e. time-of-flight) data is available. In this case, an approach based on a migration procedure, which exploits the temporal information, is more applicable. In the terahertz imaging community, analogs of each of these imaging configurations has been explored. The study of tomographic techniques using terahertz radiation has been discussed in a recent review [106].

For the purposes of this article, we distinguish tomography from the time-of-flight images discussed above according to the number of transmitters and/or detector locations that are involved in image formation. In the preceding section, all of the time-of-flight measurements involved a single transmitter and a single receiver, both at fixed locations. With multiple transmitters and/or detectors at multiple positions, an object can be illuminated from more than one location, or the scattered field from a single illumination point can be detected at multiple locations. This is essence of a tomographic measurement. In practice, most terahertz tomographic measurements have involved a single transmitter–receiver pair, with multiple positions of one or the other (or both) measured serially and with the data subsequently assembled into an image. The advent of fiber-coupled terahertz photoconductive transmitters and receivers was a crucial step in permitting further developments in terahertz tomography, because it enabled the rapid repositioning of the photoconductive antennas without loss of optical alignment or temporal delay calibration [107].

The first demonstrations of a terahertz tomographic measurement, according to this definition, were in 2001, shortly after the fiber-coupled antennas became available. Ruffin and colleagues measured the diffracted field transmitted through a patterned two-dimensional aperture at many locations after the aperture, and then back-propagated these measured fields using the Kirchhoff diffraction integral to reconstruct the aperture pattern [108, 109]. This group has subsequently extended this work to demonstrate reconstruction in three dimensions [22].

At roughly the same time, Dorney *et al* used an analog of seismic reflection tomography to demonstrate image reconstruction by Kirchhoff migration [19, 110], an approach commonly used in the seismic imaging community. Because of the strong similarities between sub-picosecond THz pulses and the seismic impulses used for geophysical studies, one can take advantage of a mature set of existing algorithms for image formation. These algorithms are based on much of the same underlying physics as in the case of electromagnetic propagation,

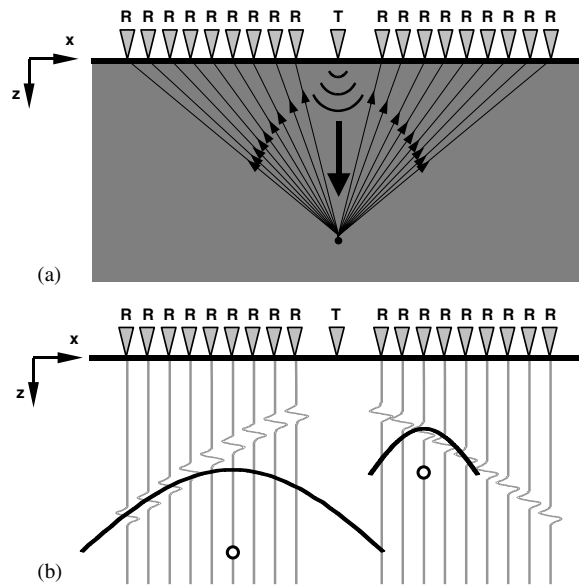


Figure 15. (a) A schematic of the seismic imaging arrangement emulated by the terahertz system. Multiple symmetrically placed receivers are arranged to collect a series of reflected waveforms from a point scatterer. The travel time increases hyperbolically with the transmitter-receiver offset. (b) Kirchhoff migration reconstructs the location of the scatterer by calculating the appropriate hyperbola and summing the recorded values along that hyperbola, for each possible scatterer location. Incorrect locations generate small summations, since their hyperbolae do not pass through many reflected pulses. Two such incorrect guesses, and their associated hyperbolae, are shown. Adapted from reference [110].

in the sense that both are direct consequences of the description of wave propagation using Green's functions. In the present case, however, some simplifying assumptions can be made because the propagating wave has the form of a broadband transient. In essence, the migration approach places more significance on the *travel time* than on the *amplitude* of the measured wave, and in doing so ignores frequency-dependent absorption and dispersive effects as well as the vector nature of the fields. This approximation neglects important aspects of the collected data, so it necessarily reduces the quality of the generated image. It leads, however, to an imaging algorithm that is very simple to implement and is extremely robust against losses due to scattering or absorption of the propagating wave. For this reason, it is well suited for image formation in situations where the THz wave must propagate through a lossy or disordered medium either before or after interacting with the target. A situation of this sort would, of course, be very challenging to handle using the conventional approach.

Figure 15(a) illustrates the configuration of the transmitter and array of receivers, mimicking a seismic tomography arrangement. The task in migration is to transform a data set collected in this way, knowing only the position of the transmitter and receivers and the travel times of the reflected pulses, into a useful image. In other words, given that the horizontal surface is the x -axis and depth is the z -axis, we wish to transform data in the (x, t) domain into the (x, z) domain. The emitted spherical wave front propagates downward, until a portion of it interacts with a point diffractor, generating a reflected wave. Given that the point scatterer is located at (x_0, z_0) , the transmitter is at $(0, 0)$, and a receiver is at $(x, 0)$, the travel time in a homogeneous medium is found from simple geometric

considerations:

$$D(x) = v_0 \tau = \sqrt{x_0^2 + z_0^2} + \sqrt{(x - x_0)^2 + z_0^2}. \quad (1)$$

Here v_0 is the velocity in the medium, τ is the two-way travel time, and $D(x)$ is the total distance from transmitter to target to receiver. A series of waveforms, measured at each of the receiver locations shown in figure 15(a), must therefore show a hyperbolic dependence of THz pulse arrival time on receiver offset (i.e. transmitter-to-receiver distance), as illustrated in figure 15(b).

The image reconstruction procedure exploits this hyperbolic dependence as follows. For each possible location (x_0, z_0) of a reflector in the plane, we compute the hyperbola that would result if a reflector was actually located there. We then determine the amplitude of the measured THz waveform at each time delay along that hyperbola, and sum these to produce a pixel value for the (x_0, z_0) location in question. Correctly guessed points yield a large summation value since the corresponding hyperbola passes through the peaks of multiple waveforms. Incorrectly guessed points result in smaller values due to the low amplitude of the waveforms intersected by the hyperbola, and due to destructive interference from different waveforms in the summation. In this fashion, an image can be assembled from the measured data. This procedure works for surfaces as well as for isolated point reflectors, and can be used to rapidly reconstruct complicated reflecting surfaces.

Two incorrectly guessed points are shown as circles in figure 15(b). The hyperbolas associated with each of these points are centred above the circles. Both points have a small valued summation due to partial destructive interference. Some of the temporal waveforms have negative amplitude values at the points where they intersect the hyperbola, while others have positive amplitude values at the intersection points. The right-hand point is closer to the surface ($z = 0$); therefore, its associated hyperbola has more curvature than the one on the left. These examples illustrate how even incorrect locations can generate non-zero amplitudes in the migration procedure and introduce image artefacts. As the number of waveforms included in the summation increases, the amplitude of these artefacts decreases.

The resolution limits of migration tomography are different for the dimensions parallel and perpendicular to the receiver array. The horizontal resolution is the smallest feature that can be resolved along the x -dimension (parallel to the array of receivers). It is generally defined in terms of the first Fresnel zone. Traditionally, the Fresnel zone is the size of an opening in an infinite plate such that only positive values of an incident spherical wave are able to penetrate the opening [111]. For a broadband source, the Fresnel zone can be defined by the size of an aperture which maximizes the transmitted energy [112]. The size of the first Fresnel zone is given approximately by

$$\Delta x = \frac{v_0}{2} \sqrt{\frac{\tau}{f_{\text{mean}}}}, \quad (2)$$

where f_{mean} is the mean frequency of the THz source and v_0 and τ are as defined in equation (1). A feature that is smaller than the size of the first Fresnel zone cannot be resolved. As the feature size increases beyond the size of the first Fresnel zone, the image reconstruction provides a better representation.

The vertical resolution is defined by the smallest feature that can be resolved along the z -dimension (the propagation direction of the incident wave). This depends on the coherence length of the probing wave. A shift in position of a temporal waveform by an amount that is small compared with the duration of the THz pulse has no significant effect on the summation. Consequently, the migration summation is not sensitive to temporal shifts of this magnitude.

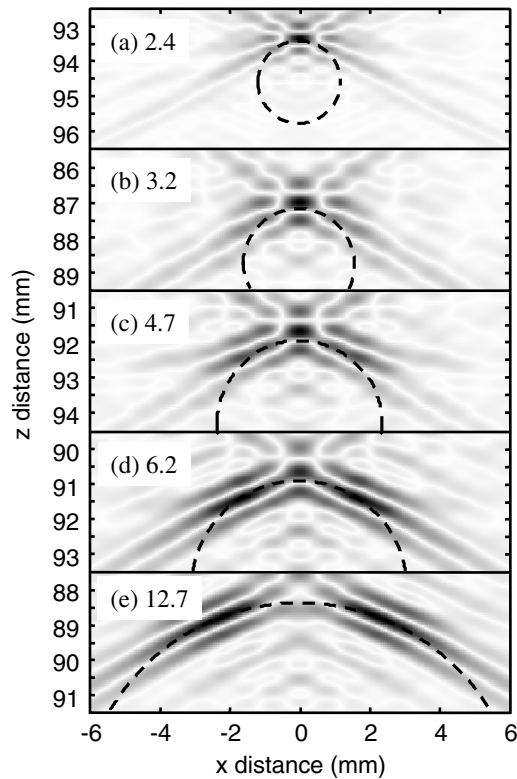


Figure 16. Kirchhoff migration images of a series of metal cylinders, with diameters as shown (in millimetres). The dashed curves represent the outlines of each of the targets, showing their sizes and actual locations, for comparison with the migration images. In (a) and (b), the objects are correctly located but their surface curvature cannot be resolved. In (d) and (e), the surface curvature is resolved over a portion of the reflector's surface, limited by the finite range of receiver offsets (i.e. finite detector aperture). Adapted from [110].

The generated images exhibit blurred edges, due to the finite coherence length of the radiation. Vertical resolution is therefore proportional to the coherence length and therefore inversely proportional to the spectral bandwidth Δf :

$$\Delta z = \frac{v_0}{4\Delta f}. \quad (3)$$

Figure 16 shows a series of images which demonstrate both the horizontal and vertical resolution limits of this technique, using metal cylinders of various diameters. Each cylinder is placed approximately 90 mm away from a fixed THz transmitter. A series of 152 reflected waveforms are collected on either side of the transmitter in 1 mm steps. The smallest transmitter-to-receiver offset is 38 mm, limited by the size and orientation of the antenna housings. Images are formed from the resulting set of waveforms using the migration procedure outlined above, for five cylindrical targets with various diameters. The vertical axes show the distance from the transmitter, while the dashed circles show the actual positions and cross-sections of the targets. For all five images, a grid spacing (pixel size) of $50 \mu\text{m}$ is used for the image reconstruction. The migration results coincide well with the actual locations of the objects.

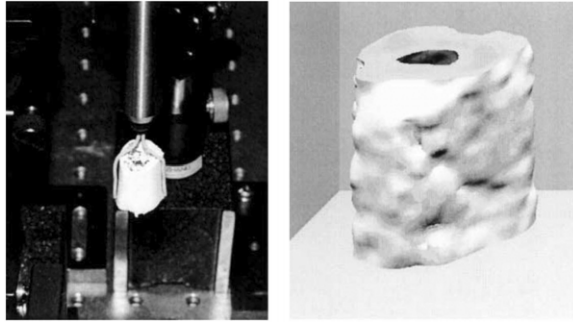


Figure 17. A photograph and a reconstructed terahertz image of a piece of a turkey bone, imaged using terahertz computed tomography. The reconstruction used the filtered back-projection algorithm. Features larger than ~ 0.5 mm are resolved in this image. Adapted from [21].

We note that the two smallest cylinders are accurately placed but are not well resolved. The diameters of these cylinders are very close to the horizontal resolution. For our measurements, the size of the first Fresnel zone is $\Delta x \sim 2.9$ mm, using equation (2). For the 4.7 mm diameter cylinder, we begin to resolve features in the image which correspond with the location of the reflecting surface. The two largest cylinders have a clearly defined surface section. Only a portion of the surface is imaged due to the finite range of receivers along the x -axis. The limited number of receivers hinders complete cancellation of diffraction sums from regions without a reflector. Consequently, we observe a number of image artefacts arising from aliasing effects, as anticipated above. The reconstructed curves of the cylindrical surfaces also exhibit a finite thickness. The finite coherence length of the radiation, which limits the vertical resolution, causes blurring that is 3–4 pixels wide. The surface blurring is consistent with the calculated vertical resolution of $\Delta z \sim 0.19$ mm, according to equation (3).

In addition to the analog of seismic imaging described here, several researchers have also explored the THz analog of x-ray computed tomography (CT). ‘T-ray’ CT was first demonstrated by Zhang and co-workers [21]. There are some important differences between THz and x-ray CT, the most obvious of which is that the THz system provides both amplitude and phase information. As a result, THz CT images can contain more information about the target, such as its refractive index. Spatial resolution is determined by the same considerations as in the vertical resolution discussed above (equation (3)). An image which illustrates the capabilities of T-ray CT is shown in figure 17. The object is placed into the THz beam, scanned across the focal point, and rotated to provide many different view angles in a transmission mode. This type of image has required raster scanning, with perhaps 100×100 pixels, obtained at numerous different angles. The acquisition time can therefore be quite long, although it can be shortened considerably using chirped-pulse electro-optic sampling, as described below [29].

A description of the image reconstruction in T-ray CT imaging is instructive, as it illustrates some of the unique features relative to conventional CT. The usual radon transform can be written in a complex form, as an integral along the line connecting the source to the detector:

$$E_{\text{det}}(\omega, \theta, l) = E_i(\omega) \exp \left[\int_{L(\theta, l)} \frac{-i\omega}{c} (n(r) + i\kappa(r)) dr \right] \quad (4)$$

Here, E_i is the incident field at frequency ω , E_{det} is the detected field at the same frequency, L is the straight line connecting the source to the detector at angle θ and horizontal offset l from the rotation axis of the object and $(n(r) + i\kappa(r))$ is the (unknown) complex refractive index of the object, at position r . To reconstruct an image, one can choose any of a number of

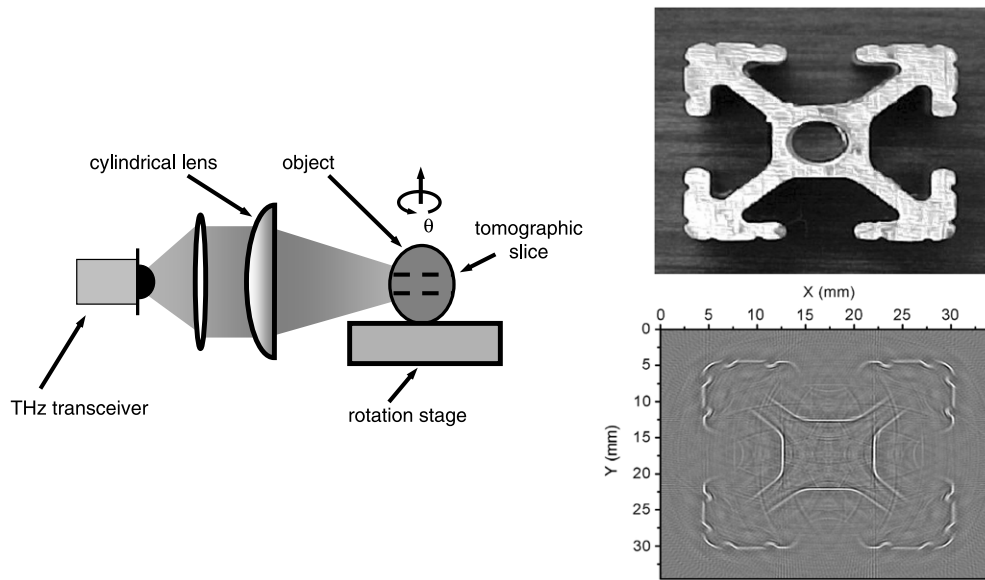


Figure 18. (left) A schematic of the experimental setup for THz wide aperture reflection tomography. A transceiver illuminates a horizontal cross-section of an object and measures the reflected radiation. In this case, the size of the illumination spot is less than 5 mm in the vertical direction and ~ 30 mm in the horizontal direction. (right) A photograph and a THz reconstruction of a complicated metal object. This image was reconstructed using 360 waveforms, collected in 1° increments as the object was rotated and then assembled using a filtered back-projection. The image reproduces the small surface features of the object, which are roughly half of the coherence length in size. Adapted from [24].

aspects of the measured data. For example, Ferguson *et al* have pointed out that one can use the unwrapped Fourier phase $\arg \{E_{\text{det}}/E_i\}$ as the basis for back-projecting an image. In this case, the filtered back-projection reconstructs the phase delay at each pixel of the image, which can then be used to compute the spatial (and spectral) variation of the refractive index [113]. More advanced wavelet-based segmentation techniques are also under investigation [114].

We have recently described a different approach using a reflection geometry, in which the THz beam is brought to a line focus, rather than a point. This wide-aperture reflection tomography permits tomographic reconstruction using a series of slices, measured at several different view angles [24]. Since this is a reflection technique, it works best with strongly reflecting objects such as metals. A schematic of this technique, along with a typical image, is shown in figure 18. The reconstruction of three-dimensional images using the filtered back-projection algorithm with a single-frequency terahertz source has also recently been reported [115].

Another tomographic technique which borrows from research in a different spectral regime is terahertz synthetic aperture imaging. Aperture synthesis is a technique commonly employed in astronomy and in radar measurements, in which the effective aperture of a measurement system is increased by reorienting the object (or relocating the detector) so that a slightly different viewing angle is accessed. If the sequential images acquired in this fashion are superposed coherently, one can obtain an image with improved resolution. The essential distinction between conventional aperture synthesis and the migration technique discussed above is in the algorithmic approach used to assemble the multiple target views into a single high-resolution image. The application of synthetic aperture radar (SAR) analysis to a terahertz imaging system has been described by Chevillat [18] and by Grischkowsky [23, 116]. An example of a THz SAR image is shown in figure 19. This shows a 1/2400 scale model of a ship, imaged

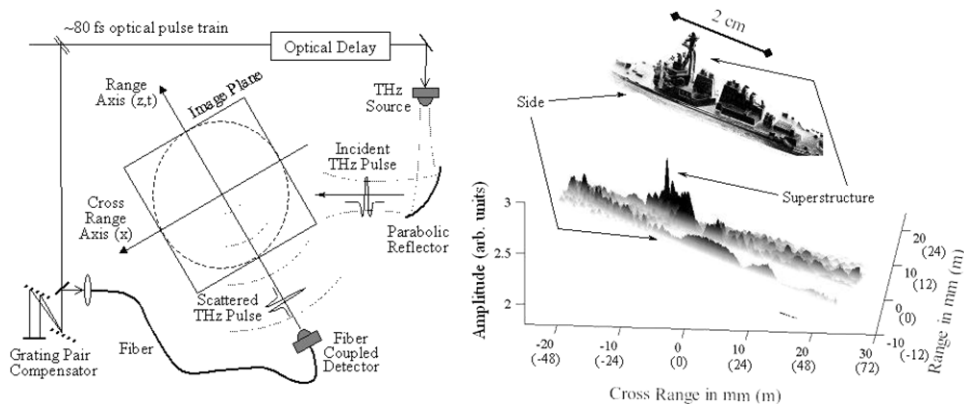


Figure 19. (left) A schematic of the experimental setup for THz synthetic aperture imaging. (right) An image of a 1/2400 scale model of a destroyer obtained with the setup shown at left. A photograph of the object is shown above the terahertz image, for comparison. The side and superstructure of the object are visible in the THz image, which was acquired with measurements spanning only a 20° angular range, in 1° increments. The axis values in parentheses are the distance in metres corresponding to the scaled image. Adapted from [18].

over a 20° range in 1° increments. In addition to showing the power of aperture synthesis in a time-domain system, this image illustrates the potential of using THz systems for scale-model experiments. The measurement of radar cross-sections of complex reflective objects is a challenging task, which can be dramatically simplified by using small scale models. In this case, the wavelength of the radiation must be scaled by the same ratio. This naturally leads one to study centimetre-scale models with sub-millimetre-wavelength radiation [117–119]. If the model is a faithful replica of the original, then the measured THz scattering properties will reproduce the results that would be obtained in a radar measurement, since the reflectivity of metallic components are very high throughout the far-infrared and microwave. For the image shown in figure 19, the frequency range of the illumination source (0.2–1.5 THz) corresponds to a scaled frequency range of 83–625 MHz, with a target-to-receiver distance of 840 m.

In an imaging configuration of this sort, just as in the migration example described previously, the resolution in the range direction and in the cross-range (perpendicular to the target-detector axis) direction are not the same. Along the detector axis, the resolution is determined by the coherence length of the radiation. In the cross-range direction, the resolution is determined by the condition that the phase shift of the radiation reaching the detector is equal to π across the effective detector aperture. This is equivalent to requiring that the target be larger than the first Fresnel zone of the incident illumination. In the imaging system illustrated in figure 19, the range resolution is roughly an order of magnitude better than the cross-range resolution, because of the large bandwidth of the THz source.

Recently, Federici and co-workers have explored further advantages of aperture synthesis using THz pulses, pointing out that a clever (non-periodic) spatial arrangement of the detectors can give a larger effective aperture and also suppress image artefacts arising from aliasing [120, 121].

2.6. Video-rate terahertz imaging and single-shot terahertz imaging

The imaging techniques described heretofore have all relied on a raster-scanning method, to acquire image data pixel by pixel. This can be a limiting factor in some applications, since

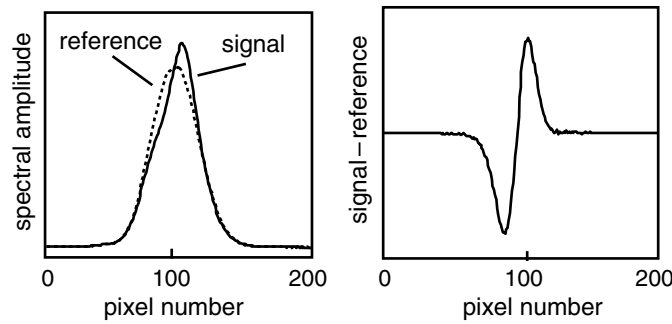


Figure 20. Spectrum of a chirped femtosecond probe pulse, after passing through an electro-optic crystal between crossed polarizers, with the terahertz beam blocked (marked 'reference') and unblocked (marked 'signal'). The spectra are different because the terahertz beam induces a polarization rotation of the probe pulse, which is mapped onto the spectrum of the probe by the linear chirp. (right) The difference between the two spectra at left is proportional to the terahertz electric field $E(t)$. This can be measured with a single pulse from the femtosecond laser. Adapted from [29].

serial acquisition of image data can be quite slow. One solution would be the development of a sensitive focal plane array detector, an area of active research [122]. Ultrafast optics offers another solution to this problem, using the free-space electro-optic sensing technique described above.

As noted, electro-optic sampling relies on an induced polarization rotation in a femtosecond probe pulse, which depends on the amplitude and direction of the terahertz field. Because the detected signal is an optical one (i.e. polarization rotation of an optical probe beam) rather than an electrical one (photo-induced current in a metal antenna), the sampled region is defined by the size of the optical probe and of the non-linear crystal rather than by the size of an antenna. So, instead of using a small electro-optic crystal and a focused THz beam, one can use a large (cm^2) crystal and a large-area beam. The spatially varying polarization rotation of the probe beam can be measured using crossed polarizers and a CCD camera [81]. Since a CCD detector array can refresh at video rates, this technique can be used to generate terahertz movies [25, 26, 123]. It does, however, require considerably more optical power in the femtosecond probe beam. Generally, an amplified femtosecond laser system is required. Also, one still requires a mechanical delay line to vary the delay between the probe pulse and the THz pulse in order to obtain a measurement of the terahertz electric field.

It is also possible to dispense with the delay line entirely and measure the full THz waveform with a single pulse from the femtosecond laser. This can be accomplished using a gating pulse which is chirped; that is, its frequency changes as a function of time. This technique was first demonstrated in the measurement of picosecond electrical pulses, using a frequency-swept DFB laser [124]. It was subsequently applied to the measurement of free-space terahertz pulses by Zhang and co-workers [27–29]. This idea relies on the fact that a controllable linear chirp can be imposed on an optical pulse, for example, using a pair of gratings. In this case, the group delay of the optical pulse is a linear function of frequency, with the high-frequency components leading and the low-frequency components trailing. If this chirped pulse copropagates with a terahertz pulse through an electro-optic crystal, each spectral component experiences a different degree of polarization rotation, as determined by the delay of that particular spectral component relative to the THz field. The modulated spectrum can then be measured using a spectrometer, and compared to the spectrum measured with the THz pulse blocked. An example of a spectrum modulated by a terahertz pulse is shown in figure 20.

The advantages of a single-shot technique for THz pulse measurement are numerous [125]. Clearly, the ability to measure individual pulses opens up a range of new possible uses for THz diagnostics. An excellent example is the work of Wilke *et al.*, who measured the THz electric field associated with a short (picosecond) electron bunch propagating in a linear accelerator [126]. Measurements of this type can be used to characterize the duration and shape of these short electron bunches, on a shot-by-shot basis. Another useful advance has been the realization that the modulated chirped spectrum can be measured with a one-dimensional array of detectors, so that the other dimension can be used to obtain spatial information. Thus, one can obtain the full temporal evolution of the THz field, not just at a single point in space, but at many points along a line, all with a single pulse from the laser. Jiang and Zhang demonstrated this spatio-temporal measurement technique by imaging the field emitted by a photoconducting dipole antenna along one dimension, in a single shot [29].

This chirped-pulse detection scheme has a few important limitations. In practice, spatio-temporal field imaging requires an amplified fs laser, because the pulse energy produced by a typical fs oscillator is not sufficient. This is not necessarily a significant disadvantage, since the lower repetition rate of the amplifier is often more suitable for the signal (or image) processing requirements, which could not be performed on a shot-by-shot basis at the high repetition rate of a typical oscillator. Of course, the need for an amplifier does increase the cost and complexity of the laser system. Another important issue concerns the fundamental limits on the temporal resolution. Since the terahertz pulse modulates only a portion of the spectrum of the visible pulse (corresponding to the portion which propagates through the electro-optic crystal at the same time as the terahertz pulse), the ultimate time resolution cannot be higher than the inverse of this bandwidth. The temporal resolution is given by the geometric mean of the duration of the chirped pulse and its original duration (i.e. before chirping) [28, 29]. For example, using a 50 fs probe pulse, chirped by a factor of 400 to 20 ps, one would find a time resolution of about 1 ps. This result limits the utility of the chirped-pulse measurement technique to some extent and can even lead to ambiguities in the interpretation of the measured modulated signal [127]. Several groups have investigated ways to overcome this resolution limit [128, 129].

2.7. Terahertz imaging with a continuous-wave source

In parallel with the rapid progress in pulsed time-domain techniques, tremendous strides have also been made in technologies for continuous-wave (cw) terahertz systems since the first examples [5, 6]. In this case, the challenge is usually related to the development of new or improved sources of terahertz radiation or new or improved detection technologies. In many cases, the use of such sources and detectors for imaging is intended merely as a demonstration of feasibility, rather than as a development of a new terahertz imaging technique. Since the purpose of this paper is to focus specifically on techniques for terahertz imaging and the applications these enable, we will avoid the temptation to discuss source and detector development. Instead, we provide a selected review of imaging results, intended to highlight the examples which illustrate novel imaging capabilities or exciting applications areas. We note that several groups have recently discussed the comparison of cw versus pulsed imaging in the THz range [70, 130].

Usually, coherent detection cannot be used to measure continuous-wave terahertz radiation. This is because, in most cases, the cw source is not synchronized (phase-locked) to an optical source that could be used for sampling. One exception is the technique pioneered by Nahata and co-workers. Here, two single-mode lasers, tuned to slightly different frequencies, were used to generate THz radiation via difference-frequency mixing in a photoconductive

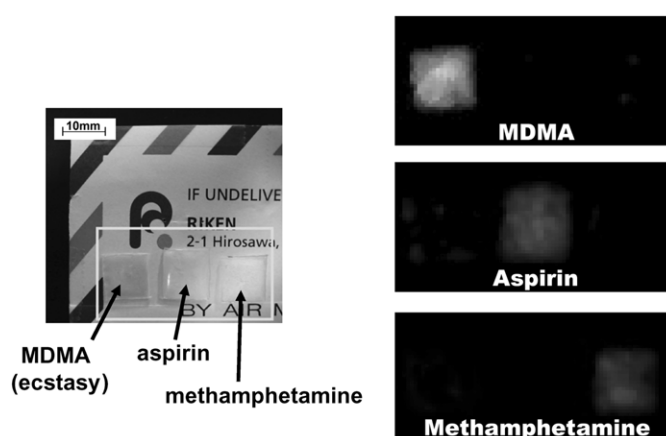


Figure 21. A visible image and a set of terahertz images showing three different powdered materials inside an envelope. At each pixel, spectroscopic information is used to identify the material, based on the known absorption signatures between 1 and 2 THz. Adapted from [39].

device. Unlike other photomixer-based terahertz imaging systems [43, 131], the terahertz radiation was detected via electro-optic sampling using the same two lasers. This process is essentially an upconversion of the THz radiation, followed by homodyne detection [132]. Because the THz radiation is phase-locked to the beat signal between the two optical sources, the process is coherent and both amplitude and phase information can be determined. This technique can be used for focal plane imaging [133], in a manner similar to the electro-optic imaging techniques mentioned earlier [81]. Similar results (although with raster scanning of the object to produce an image) can be obtained using a photoconductive mixer as the receiver [130, 134].

Another exception is the recent work of Roskos and co-workers, who have used electro-optic sensing with a femtosecond laser to measure both amplitude and phase information from a continuous-wave THz source (a Gunn oscillator at 0.6 THz). This is possible because of the extremely low jitter between the two sources, due to their intrinsic stability. This hybrid system has a number of advantages, including a high dynamic range for imaging and the elimination of the need for an optical delay line [135].

With these exceptions, cw THz imaging systems typically employ an incoherent device for direct detection of the THz wave, such as a bolometer or a Golay cell. Array detectors are also available for direct (not heterodyne) detection, including microbolometer arrays [136, 137], germanium detector arrays [138] and pyroelectric cameras. Unlike in the case of THz-TDS, the source and detector are independent devices, rather than two components of a coupled system. In some cases, the terahertz source is tunable, in which case it is possible to combine spectroscopic measurements with imaging just as in the time-domain systems. A notable example is shown in figure 21. Here, a tunable terahertz parametric oscillator and a pyroelectric detector [139] are used to image a collection of powders inside an envelope, by raster scanning the sample through the THz beam [39]. At each pixel, a spectrum is collected by tuning the source between 1 and 2 THz. These crystalline materials have unique terahertz absorption signatures in this range, even in powdered form at room temperature, which can be used for identification with a multispectral analysis [40]. The terahertz image clearly shows that the spatial location of each of the different substances can be determined. Imaging with frequency tuning over a more narrow spectral range (500–700 GHz), but with more power in the THz beam, can be achieved using a backwards wave oscillator [140].

One important advantage of imaging with a single-frequency source is the ability to select the source wavelength to optimize the imaging capability. This is relevant, for example, in the case of imaging at a stand-off distance. Stand-off imaging (i.e. at greater than a few metres distance) is challenging because of the presence of atmospheric water vapour, which significantly attenuates the terahertz beam. However, at certain frequencies within the terahertz range, the atmospheric attenuation is minimized because there are no nearby strong water vapour absorption lines. The ability to tune the terahertz source to a water 'window' is a considerable advantage. For example, for a 25 m stand-off, the power throughput from transmitter to receiver increases by more than a factor of 10 if the atmospheric loss decreases by only 0.5 dB m^{-1} . For comparison, variations of several dB m^{-1} can be achieved by frequency tuning within narrow windows in the 4–5 THz range. Real-time imaging at a 25 m stand-off has been demonstrated using a terahertz quantum cascade laser (QCL) and a room-temperature microbolometer array [122, 137]. In this demonstration, the QCL was held at 30 K, within the range of a thermomechanical cooler that does not require liquid cryogenics, and produced $\sim 17 \text{ mW}$ of power in pulsed operation. A few per cent of the emitted power reached the imaging array, sufficient for imaging with a 1 s integration time. A system diagram and sample images acquired with this system are shown in figure 22 [45]. This system can also be used for video-rate imaging [137].

It is also worth mentioning passive imaging, in which one relies on the thermal radiation from the object (or the thermal radiation illuminating the object from its surroundings or from the sky) to provide contrast. This technique has been pioneered in the astronomy community, for the obvious reason that it is not possible to illuminate astronomical objects. In this case, it is clear that the primary challenge is the development of sensitive detectors or detector arrays, which can distinguish between thermal sources differing only slightly in their absolute temperature. Heterodyne techniques are frequently used, in the cases where a strong local oscillator is available. For example, Rodriguez-Morales *et al* have developed a superconducting bolometer integrated with gain circuitry [141]. The device operates at a design frequency of 1.6 THz, with a far-infrared gas laser used as a local oscillator. To use this device for imaging, an oscillating mirror is incorporated into the optical system. This scanning mirror varies the view angle of the detector, sweeping along a line for a one-dimensional image of a target. The reported noise level corresponds to a temperature difference of about 1.5 K.

2.8. Some more examples

The possibility for using THz techniques for imaging and sensing has inspired research into many possible applications. Several of these are illustrated in the images shown earlier in this paper, but there are quite a few others. In this section, we discuss some of these other applications, most of which can be best understood from the terahertz images themselves. These pictures, and others like them, clarify much of the excitement surrounding the emerging technology of terahertz imaging.

Among the earliest published examples of an application for terahertz imaging involved the inspection of semiconductor wafers. This idea was inspired in part by the fact that many of the researchers involved in the early development of terahertz time-domain spectroscopy had backgrounds in semiconductor physics and were familiar with these materials. The terahertz properties of a doped semiconductor are well described by Drude theory [142, 143], so one can readily extract material parameters such as the doping density and the carrier mobility from terahertz measurements [144]. These two parameters can be separately determined with the use of a magnetic field, which induces a high-frequency Hall effect [92]. The study of charge carriers in semiconductors was also one of the first topics studied using near-field terahertz

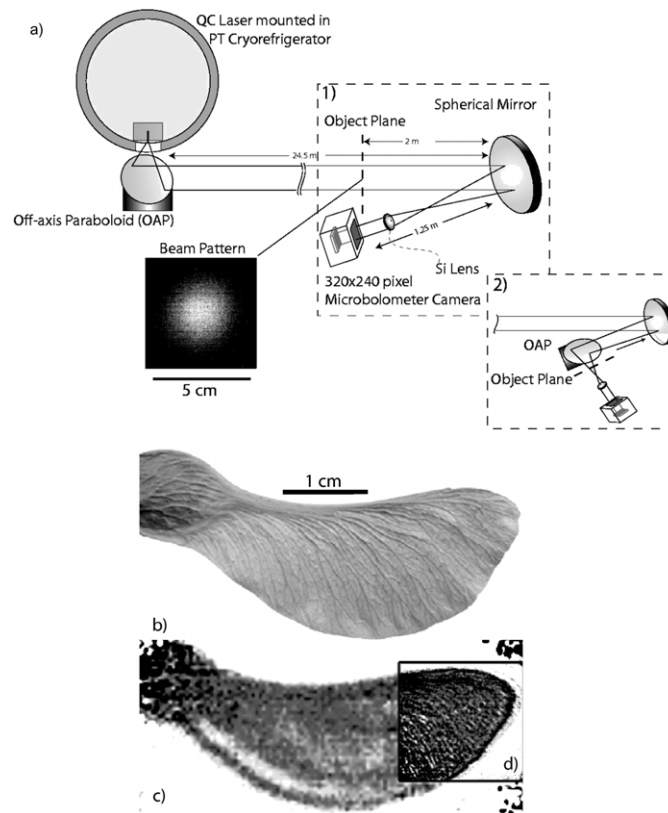


Figure 22. (a) A schematic of the optical system for THz transillumination imaging with a 25 m path between the source and the detector array. The dashed lines show two different optical configurations, with different locations for the sample plane. (b) An optical image of a seed pod, the sample used to demonstrate the imaging capability. (c) A THz image of the seed pod, using optical configuration #1. (d) a higher resolution image (~ 1 mm resolution) with a smaller field of view, obtained using configuration #2. Adapted from [45].

imaging [145]. However, this characterization technique has not yet seen widespread use in the semiconductor industry, in part because other options exist for wafer inspection.

In contrast, the idea of using terahertz imaging for security screening applications is very compelling because there are few other options which offer the capabilities of terahertz technologies. For obvious reasons, new methods for imaging and sensing which can enhance existing security systems are of considerable interest. The ability of terahertz radiation to penetrate many common non-metallic materials, combined with the possibility for spectroscopic identification of sensitive materials, has inspired a great deal of research. Here, we provide only two examples to illustrate the potential uses of terahertz imaging for security screening. Figure 23 shows a terahertz image, taken in a transmission geometry, of a briefcase containing a knife. For this data, the terahertz source was a solid state device (a Gunn diode with frequency multiplication) operating at 200 GHz. The detector was a Schottky diode, and the object was raster scanned in front of the terahertz beam [146]. The appeal of this image is clear, although many challenges remain before field tests are feasible. For example, the image acquisition rate is still too small for video-rate detection. A second example, shown in figure 24, demonstrates the ability to see through the sole of a shoe and identify objects



Figure 23. A photograph and a terahertz transmission image of a briefcase containing a large knife. This image was obtained with a narrow-band continuous-wave terahertz source, operating at 200 GHz. It illustrates one of the possible applications of terahertz techniques in security screening applications. Adapted from [146].

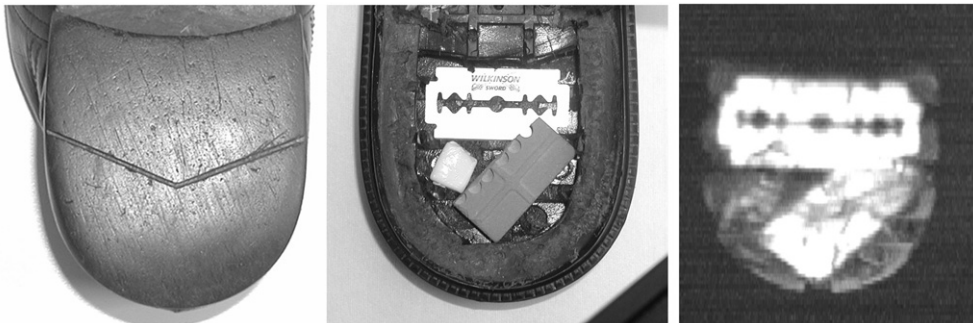


Figure 24. Photographs of the sole of a shoe and of the objects hidden inside. The terahertz image (right) demonstrates the ability to detect and identify hidden objects, in this case a razor blade, a ceramic block and a small square of a plastic explosive material. This image was obtained using a time-domain spectrometer and could therefore also contain spectroscopic information which could be used to identify the chemical composition of the explosive. Image courtesy of P Taday and M Pepper, Teraview Ltd.

hidden inside, including a razor blade and a plastic explosive. This image, obtained with a pulsed time-domain system, can also in principle contain spectroscopic information which would permit identification of the chemical compounds in the hidden materials. Identification of explosives using terahertz reflectance spectroscopy has been demonstrated by several groups [95, 147, 148].

Another forefront research area is the use of terahertz techniques for medical diagnostic purposes. This concept is limited by the strong absorption of liquid water at all frequencies

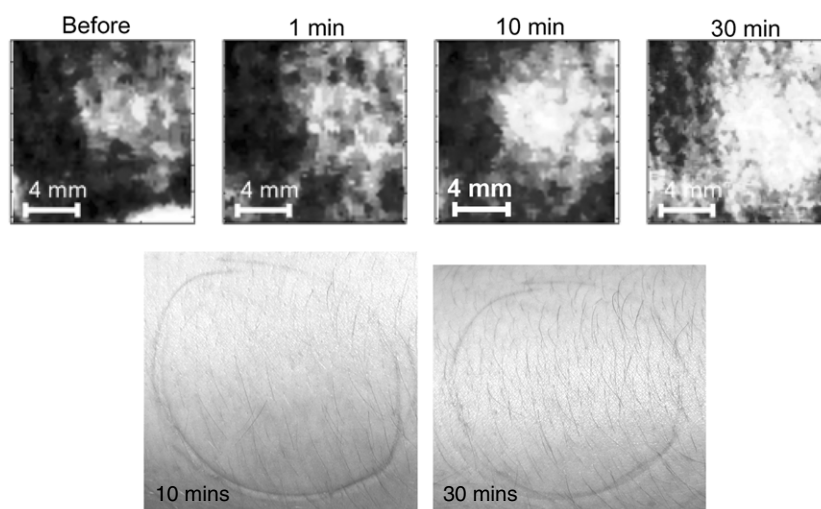


Figure 25. (top) A series of terahertz images of a volunteer's arm, imaged before and in the moments after the application of a freezer burn. The photographs (bottom) show no evident change to the skin's surface, but the terahertz image clearly identifies the growth of a sub-cutaneous oedema (a fluid build up) after several minutes. Image courtesy of P Taday and M Pepper, Teraview Ltd.

in the terahertz range, which restricts the penetration of terahertz radiation into living tissue. Even so, there are several important problems for which terahertz imaging may be a useful diagnostic [149]. The most prominent of these is the study of sub-cutaneous skin cancer, a topic under intensive study for the last several years [94, 113, 150–153]. An example of a similar application is shown in figure 25. Here, a volunteer was subject to a mild freezer burn on exposed skin and then monitored using terahertz reflection imaging for up to 30 min after the burn. Although no changes are visible in the photographs of the burned area, the terahertz image detects an oedema (sub-cutaneous fluid buildup) resulting from the burn. This result demonstrates the capability of terahertz radiation to penetrate the stratum corneum (the outermost skin layer) and provide information about the layers underneath. Other biomedical applications under study include the diagnosis of tooth decay [149, 154], the characterization of human bone [155] and (using near-field techniques) the observation of ionic flow in heart muscle fibres [156].

Rather than seeing the sensitivity to water as a disadvantage, one can also imagine using terahertz imaging to quantify the water content in biological tissue. This idea was first illustrated in the measurement of the water status of living leaves [15]. Figure 26 shows a pair of images of a living leaf, showing the water distribution and its variation with time after the plant was watered. Currently, there is no accepted, non-destructive procedure for measuring the leaf water status of a transpiring plant. Research in the field of plant water relations has been limited to point-in-time observations that provide average values across the tissue being studied. Multiple spatial and repeated temporal observations have been required to account for the dynamic movement of water through plants and for spatial variation in water status in individual leaves. Using THz imaging, it is possible to account for inhomogeneities in the sample by performing a spatially resolved measurement. Because these measurements are inherently non-destructive, repeated measurements may be made on the same tissue, thereby providing for the study of water flow dynamics [15, 157, 158]. Another evocative image which illustrates the transparency of common objects and the opacity of liquid water is shown in figure 27, a whimsical example that needs little explanation.

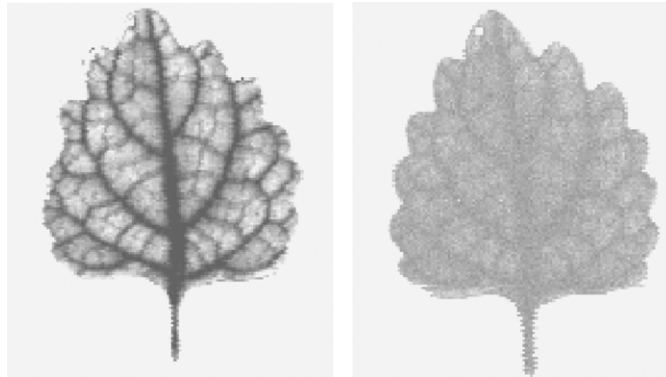


Figure 26. Terahertz images of a living leaf on a plant. In this measurement, the plant was first starved of water for several days, and the leaf was imaged (left image). Subsequently, the plant was watered. Several tens of minutes after watering, the water distribution in the leaf is much more uniform, indicating a dynamic uptake of water (right image). This demonstration is of particular interest, because no other non-destructive method exists for monitoring the water status and water distribution in living leaves.



Figure 27. A terahertz image of a teapot, taken at 200 GHz using a Gunn diode and a Schottky diode detector. Image courtesy of X-C Zhang, Rensselaer Polytechnic Institute.

Another challenging area which is ideally suited for terahertz imaging is the identification of defects or inhomogeneities in foam insulation or foam padding. This class of problems is of particular interest because there are few alternative methods that can be used for this purpose. Detecting an air bubble defect in a foam block is challenging because foams are mostly air. However, in the terahertz range, there are several different contrast mechanisms. Since foam is a low-density air-polymer composite, the refractive index is quite small (typically ~ 1.02) [68], so the extreme sensitivity of the time-domain systems to small changes in propagation delay is valuable in this case. Also, because the air voids in a typical foam composite are often comparable in size to the terahertz wavelength, they can induce moderate scattering losses which can be used as an amplitude contrast mechanism. An example is shown in figure 28. This shows a portion of an automobile dashboard, which consists of a pair of opaque plastic layers, sandwiching a ~ 1 cm thick foam layer. The terahertz image, obtained in transmission using amplitude contrast, is easily able to locate an air bubble in the foam [75]. Another

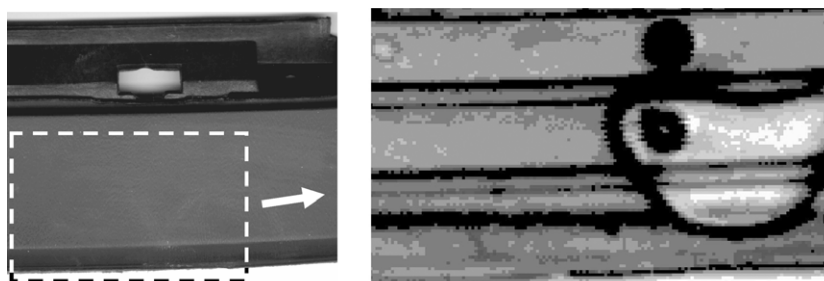


Figure 28. A photograph (left) and a terahertz image (right), obtained in transmission, of a portion of an automobile dashboard. The dashed rectangle shows the region of the terahertz image. An air bubble in the foam, invisible in the photograph, is easily identified in the terahertz image as a region of enhanced transmission. This defect could also be identified from variations in the transit time of the terahertz pulse through the sample. The horizontal dark lines in the terahertz image arise from diffraction off of edges of the plastic cover on the back side of the sample, not shown in the photograph at left. Similarly, the black circles are screw holes in the plastic cover on the back of the object. Adapted from [75].

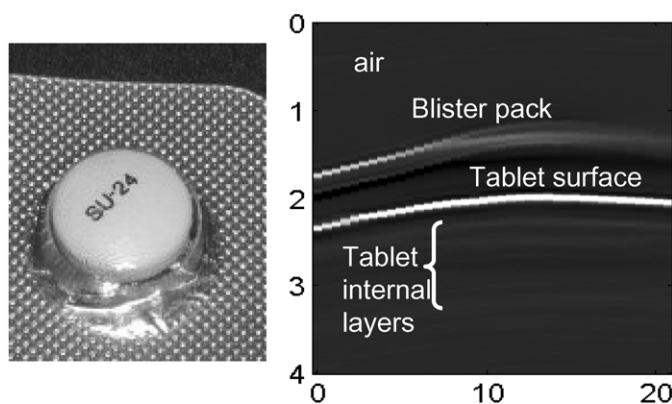


Figure 29. A photograph (left) and a terahertz time-of-flight image (right) of a medicine tablet, imaged while still inside the blister pack (as shown). The reflected pulse contains information about the internal (buried) interfaces arising from the multi-layered structure of the tablet. Image courtesy of P Taday and M Pepper, Teraview Ltd.

prominent recent example is the location of defects in the spray-on foam insulation used to protect the space shuttle. These can be located using either a time-domain system [159] or using a narrow-band cw source [146].

The possibility to perform time-of-flight measurements has inspired a number of different ideas in the general area of non-destructive evaluation. An interesting example is illustrated in figure 29, which shows a terahertz image of a medicine tablet. This shows a time-of-flight image (similar to the lower image in figure 12), which displays the reflecting surfaces encountered by the terahertz pulse, including several internal surfaces inside the tablet [160]. This image was acquired with the tablet still contained inside its blister pack; the reflection from this plastic container is also visible in the image. When combined with the spectroscopic capability of broadband terahertz systems, such as the ability to identify chemical species and polymorphs [161, 162], this technique offers a valuable new tool for quality control in the pharmaceutical industry. There have been numerous other examples of problems in

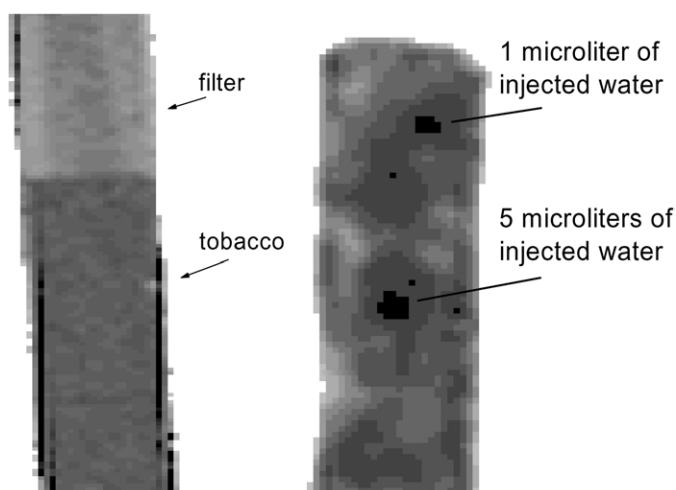


Figure 30. Two terahertz transmission images of cigarettes, measured with a time-domain system. Both of these images show the peak-to-peak amplitude of the terahertz pulse at each pixel. In the image at left, the grey scale is calibrated so that the transmission through the filter and through the tobacco can be clearly distinguished. The tobacco transmits less terahertz radiation because it has a higher water content. At right, small quantities of liquid water have been injected into the shaft (the tobacco) of the cigarette at two locations, using a micro-pipette. These are easily located by the diminished transmission of terahertz radiation.

non-destructive evaluation which are amenable to terahertz imaging. Brucherseifer *et al* have measured the thickness uniformity of thin oxide layers in fuel cells [163]. Several groups have studied the thickness and uniformity of paint layers on metal surfaces, as well as detecting hidden corrosion [50, 164]. Recently, Yasuda *et al* have demonstrated a real-time (10 frames s^{-1}) line-scan imaging system for *in situ* monitoring of the thickness of paint during the drying process [165].

Finally, numerous applications have been explored which exploit the transparency of common materials as well as the capability of a pulsed TDS system to measure both amplitude (i.e. absorption) and phase (which is often correlated with density). In many cases, the applications are fairly 'low-tech' problems, for which there may only be a 'high-tech' solution. As an example, figure 30 shows two terahertz images of cigarettes. In these and many other packaged consumer products, one can make simultaneous measurements of moisture and density. This information is not easily obtained using other technologies. In certain cases, competing technologies such as beta gauges pose a health hazard to workers and demand considerable expense and effort in regulatory compliance. Terahertz radiation is, of course, utterly benign, especially at the microwatt (or smaller) power levels of a typical THz-TDS system. Another interesting example is the study of tree rings using terahertz imaging, a non-destructive evaluation technique which can provide equivalent information to the more customary method which involves destroying the sample [166].

3. Terahertz imaging below the diffraction limit

One of the clear limitations of all of the terahertz imaging techniques described so far is the spatial resolution. With a diffraction-limited optical system, the spot size of a focused beam is roughly equal to the wavelength multiplied by the f -number of the focusing optics. As a result,

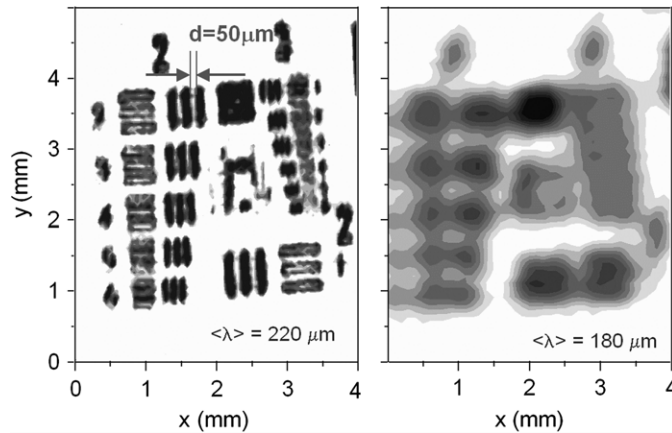


Figure 31. Terahertz transmission images of a resolution target (gold lines on a high-resistivity silicon substrate), obtained using a diffraction-limited optical system (right) and using a tapered conical near-field probe with an aperture of $\sim 50 \mu\text{m} \times 80 \mu\text{m}$ (left). The mean wavelength of the radiation (as shown) changes because of the frequency-dependent transmission of the near-field probe. In the left image, the resolution is determined by the size of the aperture and is better than $\lambda/4$. Adapted from [30].

the smallest resolvable features in an image are not generally smaller than the wavelength. For radiation at $\nu = 1 \text{ THz}$, one finds a spatial resolution ($\sim 0.5 \text{ mm}$) which is comparable to the resolution of the human eye. Terahertz images can be visually evocative because they typically show features that our eyes could see. Yet, this resolution limits the applicability of THz imaging, since smaller objects cannot be resolved or studied in any detail. Just as in the case of optical imaging [167], there is a clear motivation to push the resolving power below the wavelength limit.

As is well known in optics, one cannot create images with sub-wavelength resolution because propagating waves diffract. In order to image a small (sub-wavelength) object, one must collect not only the propagating waves but also the evanescent waves that only exist in a region very close to the object itself. Of course, evanescent waves do not propagate, so one must be very close to the object in order to measure them. A variety of techniques have been developed for optical near-field imaging, most of which involve placing some kind of probe very close to the object (within a wavelength). Since the first demonstration of terahertz sub-wavelength imaging in 1998 [30, 168], the study of near-field techniques has become one of the most active research areas in the terahertz community. As in many of the cases discussed earlier, we find that some of these efforts involve the application of these established optical techniques to the terahertz domain, while others have been developed specifically for terahertz imaging. An interesting example which does not involve a near-field probe is terahertz emission imaging (see section 3.4), a technique which is unique to the terahertz domain.

3.1. Terahertz near-field imaging with a sub-wavelength aperture

The earliest demonstration of near-field imaging with terahertz radiation used a sub-wavelength aperture to restrict the size of the terahertz illumination spot [30], as previously described in the optical regime [167] and in the mid-infrared [169]. In this case, the aperture was a tapered conical metal tip, with a sub-wavelength opening at the narrow end. A planar object scanned in front of this aperture could be imaged with a resolution determined by the size of the aperture rather than the wavelength of the radiation (see figure 31). Of course, the object must be held

within a wavelength of the aperture, so that the radiation interacts with it before diffracting. Unlike in the scanning near-field optical microscope (SNOM), this constraint does not require piezo-electric control of the aperture–sample distance, since the wavelength is so much larger. In this case, the sample was in mechanical contact with the tip, although some degree of near-field resolution could be maintained to beyond $100\ \mu\text{m}$ tip–sample separation. Aperture-based THz near-field imaging has been recently used to study ion flow in heart muscle tissue [156]. In addition, one can exploit the exponential decay of the evanescent field to perform sensitive absorption spectroscopy in the near field [35].

The sub-wavelength size of a THz receiver can be exploited, in combination with a small aperture, to provide a unique collection-mode near-field technique. This was first discussed by Mitrofanov and colleagues, who developed a collection-mode system in which a small aperture was fabricated near the collection region of a photoconductive antenna. In this case, the antenna is only sensitive to radiation impinging through the aperture, which can be much smaller than the wavelength [32, 170]. This arrangement is an improvement over the conventional collection-mode near-field system, because the detector is in the near field of the collection aperture. Thus, evanescent waves propagating through the aperture can be detected. An additional advance is the design of a dielectric protrusion through the aperture, which improves the aperture transmission even further. For imaging, the object can be raster scanned in the near field of the aperture, as in the SNOM arrangement. A spatial resolution as small as $7\ \mu\text{m}$ at 0.2 THz (better than $\lambda/200$) could be achieved [171].

A variation of an aperture-based technique, which has no analog in the optical domain, is the dynamic aperture, first described by Zhang and co-workers in 2000 [31, 172]. Here, an optical gate beam is used to photogenerate carriers at a semiconductor surface, some tens of picoseconds prior to the arrival of the THz pulse. The optical beam is focused to a much smaller spot size than the terahertz beam, so only a small portion of the terahertz beam interacts with the hot carrier distribution. The optical gate beam is modulated with an optical chopper, and the THz wave is detected using a lock-in amplifier referenced to the chopper frequency. In this way, only the small portion of the THz beam which interacts with the photoexcited region of the surface is detected. The spatial resolution is determined largely by the size of the optical spot and thus can be as small as a few tens of micrometres. This technique has recently been extended to include polarization contrast, using continuous-wave THz sources [173].

The limit of any of these techniques is determined by the amount of light that is transmitted through the aperture. The power transmission of a circular aperture decreases roughly as the sixth power of the aperture diameter d [174, 175]. In [30], the aperture attenuated the overall THz signal by more than a factor of 100. At a certain point, the transmission of the aperture must decrease to a point where imaging is no longer feasible. There may be ways to mitigate this effect to some extent, however. Nahata and colleagues have recently demonstrated the resonant enhancement of transmission through isolated sub-wavelength apertures resulting from carefully designed corrugations on the metal surface in the vicinity of the aperture [176]. This enhancement is a result of the excitation of surface plasmon modes and can be tuned to respond to specific terahertz frequencies. Using this idea, Ishihara *et al* have demonstrated near-field imaging with enhanced signal-to-noise [177]. By integrating a bow-tie-shaped aperture into the centre of a surface plasmon bulls-eye structure, one can exploit a field enhancement near sharp metal tips to couple radiation through the aperture more efficiently. With a continuous-wave THz source at $\lambda = 207\ \mu\text{m}$, imaging with $12\ \mu\text{m}$ resolution ($\lambda/17$) was demonstrated [178].

In addition to the steeply decreasing aperture transmission with decreasing aperture size, effects arise due to the frequency-dependence of the transmission. In essence, the aperture can be thought of as a cylindrical metal waveguide. This type of waveguide has a well-known

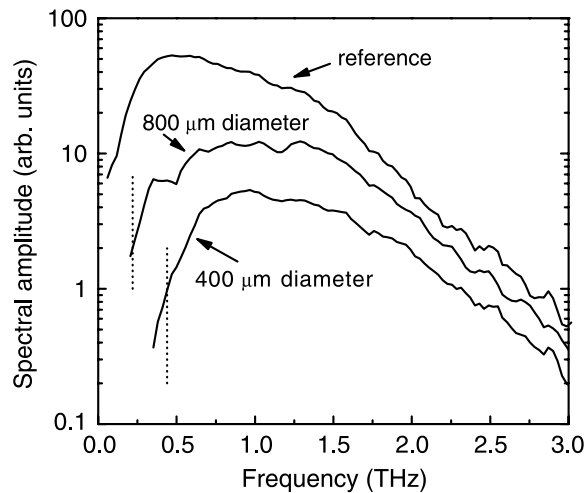


Figure 32. Spectra of THz pulses after propagation through small circular apertures in a metal screen, plotted on a log scale. The diameters of the apertures are shown. Also shown is a reference spectrum, obtained with no aperture in the beam path. The vertical dotted lines indicate the waveguide cutoff wavelength for each aperture, as given by $\lambda_C \approx 1.7d$. The spectrum for wavelengths $\lambda > \lambda_C$ is severely attenuated.

cutoff at a wavelength of $\sim 1.7d$. For wavelengths longer than this cutoff wavelength, the transmitted power is severely diminished. As an example, figure 32 shows the spectra of terahertz pulses after propagating through several small (but not extremely small) apertures. The vertical dotted lines indicate the expected waveguide cutoff frequency for each aperture. Evidently, the waveguide cutoff is the most significant factor in reshaping the spectrum of the incident radiation. In addition, wavelengths close to (but shorter than) the cutoff can experience both strong group velocity dispersion and also strong diffraction, both of which can lead to measurable pulse reshaping [30, 179, 180]. Of course, with a sufficiently high-power terahertz source, one can push the limits of the aperture attenuation significantly. A synchrotron source, for example, has been used to image biological samples with a resolution of better than $\lambda/10$ [36].

3.2. Apertureless near-field terahertz imaging

An increasingly popular alternative to aperture-based near-field techniques is a so-called apertureless near-field configuration. Originally developed by several groups in the 1990s [181–185], the implementation of this imaging method in the THz range was first reported by Planken in 2002 [33] and by Kersting in 2003 [34], using two slightly different methods. This research has illuminated several new aspects of the apertureless approach that were previously unclear. It has also been the basis of the only sub-micrometre-resolution imaging demonstration in the terahertz regime, as well as the only sub-wavelength terahertz spectroscopic measurement.

The principle of apertureless near-field scanning optical microscopy (ANSOM) is illustrated in the left-hand part of figure 33. A sharp metal probe is held close to a surface and illuminated by a focused optical (or, in this case, terahertz) beam. The metal tip vibrates parallel to the surface normal with a small amplitude, so that a small portion of the scattered radiation is modulated at the vibration frequency. This portion of the scattered radiation is

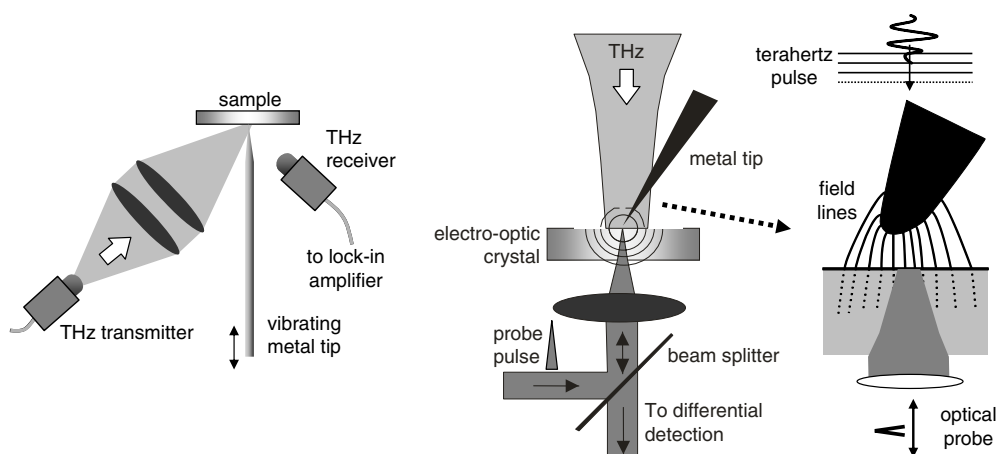


Figure 33. (left) A schematic of the conventional experimental arrangement for apertureless near-field microscopy, as pioneered by Inouye and Kawata [181] and as implemented in the THz range by several groups [34, 37, 204]. (right) A schematic of the experimental arrangement for electro-optic apertureless near-field microscopy. The metal tip distorts the electric field lines in the vicinity of the electro-optic crystal, so that they can be detected by an optical probe pulse, which enters the crystal from below and reflects off of the top crystal surface. Adapted from [38] and [33].

detected using lock-in techniques, providing information about only the region of the sample directly underneath the tip. If the tip is in the near field of the sample surface, then it can convert evanescent waves near the surface to propagating waves, which can then be detected in the far field. The resolution of this technique has been shown to depend on the tip size and the tip-sample separation, both of which can be much less than the wavelength of the radiation. This technique has been used to produce images with resolution of $\sim \lambda/100$ in the visible [186] and the infrared (at $\lambda = 10.6 \mu\text{m}$) [185] and $\sim \lambda/10^6$ in the microwave [187].

A second ANSOM configuration, with additional unique capabilities, is shown on the right side of figure 33. Here, instead of using a vibrating tip as a means for discriminating the near-field signal in the far field, a *stationary* tip is used to induce a local field distortion that can be measured directly in the near field. This is accomplished using an electro-optic crystal (gallium phosphide, GaP) which is oriented in a non-traditional manner. Instead of the usual $\langle 110 \rangle$ orientation, which gives the largest electro-optic signal for collinear propagation of the optical and terahertz beams, a $\langle 100 \rangle$ orientation is used. Ordinarily, this would give no signal, because in this orientation the electro-optic tensor vanishes for electric fields polarized parallel to the crystal surface [188]. However, as illustrated in figure 33, the close proximity of the metal tip to the surface of the GaP crystal induces a component of the THz field oriented perpendicular to the surface, which can be detected via the electro-optic effect. This trick has the appealing feature that it permits a direct measurement of the evanescent near field, rather than a measurement of the scattered near field which is performed in the far field. In the initial demonstration of this technique, a resolution of $\sim 8 \mu\text{m}$ ($\sim \lambda/250$) was demonstrated [33] (see figure 34). The resolution is limited by the size of the tip and the size of the focused optical beam spot inside the non-linear crystal.

These apertureless techniques hold great promise for both sub-wavelength imaging and spectroscopy in the terahertz range, although as with all probe microscopies care must be taken in interpreting the results. As pointed out by Knoll *et al*, it can be difficult to distinguish among several contrast mechanisms in an image obtained with ANSOM [187]. For example,

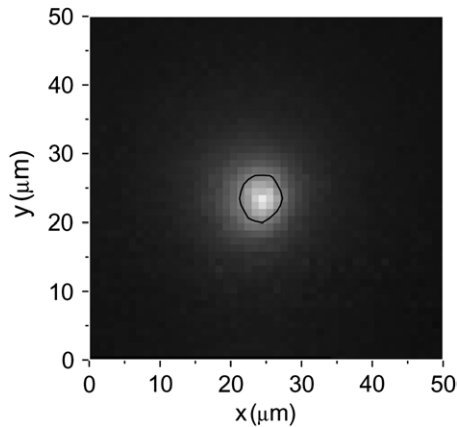


Figure 34. A sub-wavelength image of a sharp metal tip, obtained using the method illustrated on the right side of figure 33. The black circle indicates the full-width at half-maximum point of the tip image. It is roughly $6\ \mu\text{m}$ in diameter. Adapted from [33].

Chen *et al* have demonstrated sub-micrometre resolution in terahertz ANSOM imaging [34], using a sample in which the dielectric of the material beneath the tip varied in the same locations as the variations in the sample surface topography. As a result, both the tip-sample electromagnetic interactions and the tip-sample distance change simultaneously, as the tip scans across the sample at constant height. While this complicates the analysis of image data and especially the determination of spatial resolution, it is nevertheless clear from these results that imaging of nanoscale objects is feasible with terahertz radiation.

3.3. Terahertz spectroscopy and ANSOM

Of course, the ultimate goal is not merely to image such objects, but to perform spectroscopic characterization on a sub-wavelength scale. As of the date of this writing, there is only one example in the published literature of such a measurement. This result, obtained using the near-field technique shown on the right side of figure 33, is shown in figure 35. The sample is a thin CsI crystal, produced by drying a CsI salt solution on top of the GaP electro-optic sensing crystal. CsI has a well-known phonon resonance at a frequency of $\sim 1.8\ \text{THz}$ [71]. With the metal probe tip located above the CsI crystal, this resonance can be seen in the measured near-field spectrum, while it is absent when the tip is moved off of the CsI crystal, a few micrometres to one side [189]. A strong narrowband spectral feature of this sort is useful for validating the resolution of a near-field measurement.

The idea of using ANSOM for spectroscopic measurements below the diffraction limit is, of course, not limited to the terahertz domain. However, terahertz techniques have proven valuable in clarifying some important aspects of ANSOM measurements relevant to tip-enhanced spectroscopy. Here, we describe two such issues, namely, phase distortions that can result from propagation of radiation along the shaft of the metal tip and amplitude filtering effects due to the antenna response of the tip.

A common model for describing the tip-sample interaction in a typical ANSOM setup is to neglect the shaft of the metal probe, and treat the tip as a metal sphere [183, 185]. This approximation is particularly problematic in the infrared and microwave, for which it is very difficult to focus the incident beam only on the probe apex and not on the shaft. A concern which immediately arises is the influence of propagation effects of the incident radiation along

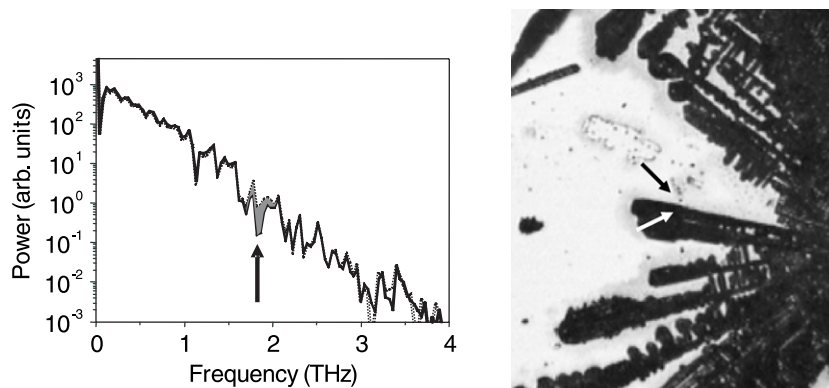


Figure 35. At right, an optical image of a gallium phosphide (GaP) surface decorated with crystals of caesium iodide (CsI), produced by drying of a CsI solution. The two spectra shown at left were obtained with the metal probe located at the two points indicated by the two arrows in the image at right, which are separated by roughly $20\ \mu\text{m}$. These spectra are nearly indistinguishable, except for a distinct absorption resonance at $\sim 1.8\ \text{THz}$, the frequency of the phonon resonance in CsI (vertical arrow). Adapted from [189].

the probe tip. These effects can influence the phase of the electric field scattered from the tip and therefore impact the results of near-field optical spectroscopy measurements [190, 191]. In order to study these phase effects, we developed a THz ANSOM system in which the illumination source and associated optics are mounted on a translation stage, so that the illumination spot can be moved along the shaft of the metal probe. In these experiments, it is impossible to focus the THz beam onto the surface without also illuminating the metal probe shaft. As a result, some of the radiation is coupled into a propagating mode on the shaft of the probe, which acts as an antenna. This propagating mode excites the tip at a delayed time and produces a scattered wave which is detected by the THz receiver. The high temporal resolution of THz-TDS makes it possible to distinguish the directly scattered field from the delayed field, scattered after propagating along the shaft of the probe tip.

Figure 36 shows a series of time-domain THz pulses, obtained by moving the transmitter stage away from the sample, so that the illumination spot moves along the shaft of the needle in steps of $1.5\ \text{mm}$. Each waveform in the plot shows the THz electric field as a function of the time delay between the optical probe pulse and the detected THz pulse. The propagation effect is evident from the relative delay of these waveforms [37]. As the point of incidence moves away from the tip, the pulse takes longer to propagate along the shaft, and its amplitude decreases. This decrease is due to the propagation loss, introduced by the finite conductivity of the shaft. From a comparison of these waveforms, it is clear that this propagation is largely non-dispersive, since the shape of the time-domain waveform does not depend strongly on propagation distance, aside from the overall attenuation.

Based on these results, it is clear that a direct illumination of the probe tip generates not only a scattered wave but also a propagating mode which is guided along the metal shaft. This mode can reflect off of structures in the experiment such as cantilevers or clamps holding the probe tip in place and return to the tip region, producing a second, time-delayed scattered wave. With an artificially constructed reflective barrier placed on the metal probe, roughly $12\ \text{mm}$ away from the tip, several such reflections can be observed in the time-domain measurements [37]. This multiple scattering produces a strong modulation of the spectral response of an illuminated tip, leading to artefacts in spectroscopic measurements. As an aside, this study also inspired

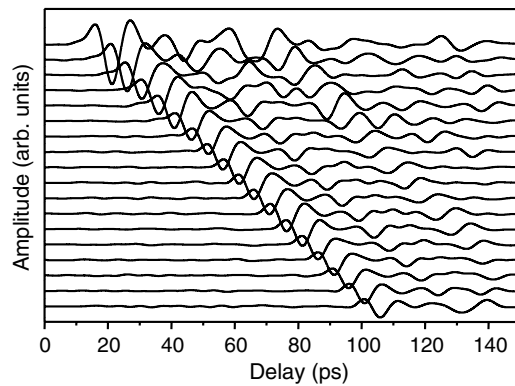


Figure 36. A series of terahertz pulses, measured for different locations of the illumination spot along the shaft of the metal probe tip in an ANSOM setup. Each successive waveform corresponds to a translation of the illumination spot by an additional 1.5 mm away from the tip. By extracting the propagation delay as a function of travel distance, it can be shown that the speed of the wave propagating along the probe tip is precisely equal to the free-space speed of light. Adapted from [37].

the discovery of terahertz waveguiding along metal wires, an area of considerable recent interest [192, 193].

An even more significant issue in the use of THz ANSOM for spectroscopic measurements involves the bandwidth-limited response of the tip-sample system. This issue first came to light when the measured time-domain waveforms were found to be quite different from the incident pulse shape [38]. This effect can be observed using both the ANSOM configurations illustrated in figure 33, which indicates that it is not an artefact associated with the scattering of the near-field signal into the far field. Results illustrating this pulse reshaping are shown in figure 37. The data on the left ((a), (c) and (e)) were obtained using the far-field measurement configuration shown on the left side of figure 33, with a bare metal substrate replacing the sample. The data on the right ((b), (d) and (f)) were measured in the near field, using the electro-optic setup shown on the right side of figure 33. In both cases, the upper two waveforms are the THz pulses incident on the tip-sample junction, while the middle two are the measured THz responses. Instead of a signal consisting of approximately a *single cycle* of the electric field, these transients consist of a positive peak, followed by a relatively slowly varying, negative tail. The frequency spectra that correspond with the measured near-field data resemble low-pass filtered versions of the incident spectra. A factor of 3 reduction in the bandwidth is observed, in both experiments.

From these measurements, an immediate and important conclusion can be drawn: in THz ANSOM experiments, the near-field spectrum *cannot be assumed* to be the same as the spectrum of the input radiation. A crucial clue regarding the explanation for the difference between the incident and the near-field signals is obtained by computing the time-integral of the *incident* THz pulse. The results are plotted in curves (e) and (f) of figure 37. These curves reproduce the essential features of the measured near-field transients, allowing for small differences in the steepness of the rising and falling edges of the main peaks. We note that integrating in the time-domain is identical to a multiplication by $1/\omega$ in the frequency domain, so the measured near-field spectra lose much of their high-frequency content.

Physical insight into the origin of this effect can be gained by employing a simple model, in which the tip is treated as an oscillating dipole. In the near field of a dipole, the electric field

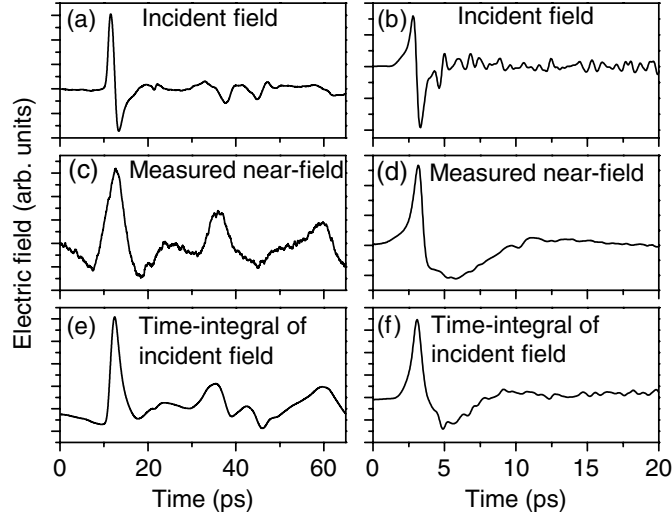


Figure 37. Terahertz time-domain pulses measured using the two experimental setups illustrated in figure 33. Curves (a) and (b) show the incident time-domain fields in the two cases, while curves (c) and (d) show the measured near-field waveforms. Curves (e) and (f) show the numerically integrated incident fields, which bear a striking resemblance to the near field results, in both cases. These reshaped waveforms demonstrate that a significant bandwidth reduction results from the use of a metal tip which acts as a resistively coupled travelling wave antenna. The curves on the left were measured in the far field using the vibrating tip method, while the curves on the right were directly measured in the near field using electro-optic sampling. Adapted from [38].

is given by

$$E_{\perp,\text{nf}} \propto \frac{\mu_0 c^2}{4\pi} \frac{p}{r^3}, \quad (5)$$

where p is the dipole moment (assumed to be oriented parallel to the vertical metal tip) and r is the distance from the dipole. Here, we have neglected terms of order $1/r$ and $1/r^2$, since in the near field these terms are small compared with the $1/r^3$ term. The continuity equation gives us a relation between the dipole moment p and the current I_{THz} in an antenna,

$$p(t) \propto \int_{-\infty}^t I_{\text{THz}}(t') dt', \quad (6)$$

where, for simplicity, the current is assumed to be the same everywhere along the antenna. A relation between the current and the incident THz electric field can be obtained by treating the antenna as a simple electronic network consisting of a radiation resistance R_r , a capacitor C and an inductance L , all in series. The driving ‘voltage’ V_{THz} of this network is the incident THz electric field E_{THz} . The relation between this electric field and the induced current I_{THz} for this network in the frequency domain is

$$I_{\text{THz}}(\omega) \propto \frac{E_{\text{THz}}(\omega)}{(R_r + j\omega L - j(\omega C)^{-1})}. \quad (7)$$

The simplest assumption is that the inductance of this antenna vanishes, and also that the capacitance is large. In this case, equation (4) can be approximated by $I_{\text{THz}}(\omega) \propto E_{\text{THz}}(\omega)/R_r$, which is equivalent to $I_{\text{THz}}(t) \propto E_{\text{THz}}(t)/R_r$. Using equations (5) and (6), this gives

$$E_{\perp,\text{nf}} \propto p(t) \propto \int_{-\infty}^t E_{\text{THz}}(t') dt'. \quad (8)$$

In the regime of resistive coupling, the near-field waveform is predicted to be proportional to the time-integral of the incident field, similar to what is observed in figure 37. In fact, with reasonable values for the antenna parameters ($R_r = 150 \Omega$, $C = 10^{-13} \text{ F}$, and $L = 2 \times 10^{-11} \text{ H}$), the spectrum of the measured near-field signal can be predicted quite accurately using equation (7) as a transfer function [38]. In retrospect, this result is not surprising from the point of view of antenna theory. The long (length $\gg \lambda$) metal tip is essentially equivalent to a travelling wave antenna. Such antennas are known to be broadband devices, with impedances that are predominantly real-valued (i.e. operating close to the regime of resistive coupling) and are in the neighbourhood of $R_r = 200 \Omega$ [194]. Significantly larger antenna resistance values have also been reported in similar THz measurements [195].

3.4. Terahertz emission imaging

An interesting variation on the theme of imaging with terahertz radiation is to directly image the emitting terahertz source. With a solid immersion lens technique, the local distribution of cyclotron radiation can be probed with $\sim 50 \mu\text{m}$ resolution [196]. This technique has proven useful in the characterization of non-equilibrium charge carrier distributions in quantum Hall devices [197].

However, this technique holds promise for even more impressive sub-diffraction-limited imaging capabilities when used in conjunction with optoelectronic terahertz sources. For example, with a photoconductive THz emitter, a focused optical beam can be used to generate charge carriers in a semiconducting substrate which then locally generate a THz pulse. This electromagnetic generation process takes place in a volume determined by the spot size of the optical beam on the semiconductor surface, which can be as small as a few micrometres. Of course, the generated THz wave rapidly diffracts to a much larger size. Even so, if one measures the emitted THz field as a function of the position of the illumination spot on the emitting substrate, one can form an emission image with spatial resolution determined by the optical spot size, not by the terahertz wavelength. This is not truly a terahertz near-field technique, since the information one obtains is not related to the spectroscopic properties of the sample in the terahertz range. Instead, it shows the ability of the sample to generate terahertz radiation, which involves the local optical absorption coefficient and the ultrafast charge carrier dynamics. Nevertheless the technique merits discussion because of the unique applicability to image formation based on terahertz radiation.

The earliest example of this emission imaging technique was reported by Brener and colleagues in 1996, in a study of the emission efficiency of structured electrodes on photoconductive substrates [198]. An illustration of this result is shown in figure 38. This image shows the enhanced terahertz signal obtained near a sharply pointed electrode, with a spatial resolution of $\sim 2 \mu\text{m}$. Subsequently, the same technique was also used to characterize the supercurrent distribution in high-temperature superconductors [199]. In this case, the maximum amplitude of the emitted terahertz radiation is proportional to the supercurrent density in the illuminated area. This distribution can therefore be imaged with a resolution determined by the illumination spot size [200]. Another recent example is from Kawase and co-workers, who have developed a laser terahertz emission microscope (LTEM) for studying the electric field distributions in integrated circuits (see figure 39) [201, 202]. This technique can be used for inspection of circuits in operation and can detect faults resulting from broken circuit lines, with a spatial resolution of $\sim 3 \mu\text{m}$ limited by the optical spot size. The LTEM technique has also been used to image hydrogen gas sensors [203].

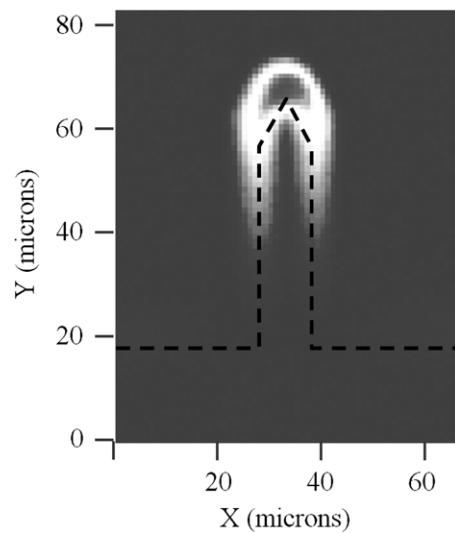


Figure 38. A terahertz emission image of a GaAs wafer patterned with a metal electrode and subject to a dc bias. The dashed line indicates the shape and location of the anode; below this line is lithographically deposited metal, while above this line is the bare substrate. The cathode, also a metal pattern, is above the field of view in this image. This image shows the spatial distribution of the terahertz emission with a $\sim 2 \mu\text{m}$ resolution. The largest THz emission comes from the pointed tip of the anode. Adapted from [15, 198].

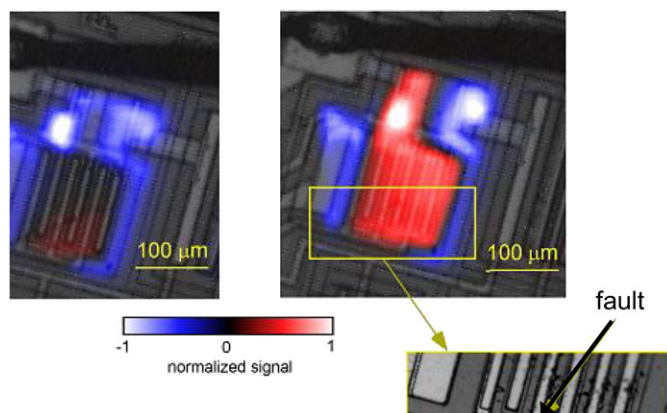


Figure 39. Two images of a portion of an integrated circuit, with superimposed terahertz emission images. The image at left is of an undamaged circuit, while the image at right shows the same circuit after one electrical line has been broken. The THz emission image changes dramatically, indicating a significant change in the electric field distribution in the operating circuit. The inset shows a close-up photograph of the region where the damaged circuit is found. Adapted from [201].

4. Conclusions

The field of terahertz imaging is extremely diverse and interdisciplinary. Terahertz science and technology lies at the intersection of several research disciplines, with distinct communities and jargon. For this reason, it can be very difficult for any one researcher to have a comprehensive view of the entire field. One is inevitably biased by the particular community from which one

originates. Nevertheless, we have tried to provide a broad view of the important developments in the field of imaging. Because of the huge range of techniques and methods, it is also challenging to go into great depths in discussions of the underlying physics in every case. We have instead chosen to provide a few key illustrative examples, along with a complete list of references which can be accessed for more information.

The growth of this field over the last few years has been motivated by a number of factors. As the least well-explored region of the electromagnetic spectrum, one may expect that spectroscopic measurements in the terahertz range will reveal new physical phenomena. In an imaging context, the significance of this factor is most clear in the pursuit of near-field techniques, which will enable spectroscopy of objects much smaller than the free-space wavelength. It is clear that the resolution and sensitivity limits have not yet been reached, and considerable research is still required to push these limits. In addition, the origin of spectroscopic fingerprints, for example, in molecular crystals, must be clarified in order to exploit these for sensing. These challenging problems are topics of current research.

Additional motivation springs from the wealth of possible imaging applications, ranging from quality control to security screening. Several of these are illustrated in this paper. In numerous cases, laboratory feasibility tests of specific imaging applications have shown great promise, and in a few cases these have led to more realistic field tests, in for example a manufacturing setting. In order for the technology to gain more widespread acceptance, a great deal of engineering research is needed. A more robust and less expensive version of a terahertz imaging system will undoubtedly enable new applications that have previously been considered unrealistic. Advances in semiconductor optoelectronics and laser sources, for example, are having a growing impact on the availability and versatility of THz-TDS systems. The terahertz field is likely to be a vibrant and active one for many years to come.

Acknowledgments

We would like to express sincere gratitude to each of the individuals who have permitted us to display some version of their data for this review. A comprehensive paper of this sort would not be possible without such generosity. This includes David Zimdars from Picometrix, Phil Taday and Michael Pepper from Teraview, Kodo Kawase from Nagoya University, Nick Karpowicz and Xi-Cheng Zhang from Rensselaer Polytechnic Institute, Paul Planken from the Technical University of Delft, Alan Cheville from Oklahoma State University, Alan Lee and Qing Hu from the Massachusetts Institute of Technology and Igal Brener from Sandia National Laboratories.

We would also like to acknowledge funding support from the US National Science Foundation, the R A Welch Foundation, the Intelligence Community Post-doctoral Fellowship Program, the National Aeronautics and Space Administration (NASA) and the American Chemical Society's Petroleum Research Fund.

References

- [1] Mittleman D 2002 *Sensing with Terahertz Radiation (Springer Series in Optical Sciences)* (Heidelberg: Springer)
- [2] Senitzky B and Oliner A A 1970 Submillimeter waves—a transition region *Proc. Symp. on Submillimeter Waves* ed J Fox (Brooklyn, NY: Polytechnic Press of the Polytechnic Institute of Brooklyn)
- [3] Gebbie H A, Stone N W B and Findlay F D A 1964 A stimulated emission source at 0.34 millimetre wavelength *Nature* **202** 685
- [4] Gebbie H A 1970 Some uses of submillimeter waves in science and technology *Proc. Symposium on Submillimeter Waves* ed J Fox (Brooklyn, NY: Polytechnic Press of the Polytechnic Institute of Brooklyn)

- [5] Hartwick T S, Hodges D T, Baker D H and Foote F B 1976 Far infrared imagery *Appl. Opt.* **15** 1919–22
- [6] Cheo P K 1978 Far-infrared laser system for detection of defects in polyethylene-insulated power cables *Opt. Lett.* **2** 42–4
- [7] Auston D H, Glass A M and LeFur P 1973 Tunable far-infrared generation by difference frequency mixing of dye lasers in reduced (black) lithium niobate *Appl. Phys. Lett.* **23** 47–8
- [8] Yang K H, Morris J R, Richards P L and Shen Y R 1973 Phase-matched far-infrared generation by optical mixing of dye laser beams *Appl. Phys. Lett.* **23** 669–71
- [9] Auston D H and Cheung K P 1985 Coherent time-domain far-infrared spectroscopy *J. Opt. Soc. Am. B* **2** 606–12
- [10] DeFonzo A P, Jarwala M and Lutz C 1987 Transient response of planar integrated optoelectronic antennas *Appl. Phys. Lett.* **50** 1155–7
- [11] Smith P R, Auston D H and Nuss M C 1988 Subpicosecond photoconducting dipole antennas *IEEE J. Quantum Electron.* **24** 255–60
- [12] Fattinger C and Grischkowsky D 1988 Point source terahertz optics *Appl. Phys. Lett.* **53** 1480–2
- [13] Fattinger C and Grischkowsky D 1989 Terahertz beams *Appl. Phys. Lett.* **54** 490
- [14] Hu B B and Nuss M C 1995 Imaging with terahertz waves *Opt. Lett.* **20** 1716–19
- [15] Mittleman D M, Jacobsen R H and Nuss M C 1996 T-ray imaging *IEEE Sel. Top. Quantum Electron.* **2** 679–92
- [16] Siegel P H 2002 Terahertz technology *IEEE Trans. Microw. Theory Tech.* **50** 910–28
- [17] Mittleman D M, Hunsche S, Boivin L and Nuss M C 1997 T-ray tomography *Opt. Lett.* **22** 904–06
- [18] McClatchey K, Reiten M T and Chevillon R A 2001 Time resolved synthetic aperture terahertz impulse imaging *Appl. Phys. Lett.* **79** 4485–7
- [19] Dorney T D, Johnson J L, Rudd J V, Baraniuk R G, Symes W W and Mittleman D M 2001 Terahertz reflection imaging using Kirchhoff migration *Opt. Lett.* **26** 1513–15
- [20] Wang S and Zhang X-C 2003 Tomographic imaging with a terahertz binary lens *Appl. Phys. Lett.* **82** 1821–3
- [21] Ferguson B, Wang S, Gray D, Abbott D and Zhang X-C 2002 T-ray computed tomography *Opt. Lett.* **27** 1312–14
- [22] Buma T and Norris T B 2004 Time reversal three-dimensional imaging using single-cycle terahertz pulses *Appl. Phys. Lett.* **84** 2196–8
- [23] O'Hara J and Grischkowsky D 2004 Quasi-optic synthetic phased-array terahertz imaging *J. Opt. Soc. Am. B* **21** 1178–91
- [24] Pearce J, Choi H, Mittleman D M, White J and Zimdars D 2005 Terahertz wide aperture reflection tomography *Opt. Lett.* **30** 1653–5
- [25] Jiang Z and Zhang X-C 1999 Terahertz imaging via electrooptic effect *IEEE Trans. Microw. Theory Tech.* **47** 2644–50
- [26] Jiang Z and Zhang X-C 1999 2D measurement and spatio-temporal coupling of few-cycle THz pulses *Opt. Express* **5** 243–8
- [27] Jiang Z and Zhang X-C 1998 Single-shot spatiotemporal terahertz field imaging *Opt. Lett.* **23** 1114–16
- [28] Sun F G, Jiang Z and Zhang X-C 1999 Analysis of terahertz pulse measurement with a chirped probe beam *Appl. Phys. Lett.* **73** 2233–5
- [29] Jiang Z and Zhang X-C 2000 Measurement of spatio-temporal terahertz field distribution by using chirped pulse technology *IEEE J. Quantum Electron.* **36** 1214–22
- [30] Hunsche S, Koch M, Brener I and Nuss M C 1998 THz near-field imaging *Opt. Commun.* **150** 22–6
- [31] Chen Q, Jiang Z, Xu G X and Zhang X-C 2000 Near-field terahertz imaging with a dynamic aperture *Opt. Lett.* **25** 1122–4
- [32] Mitrofanov O, Brener I, Harel R, Wynn J D, Pfeiffer L N, West K W and Federici J 2000 Terahertz near-field microscopy based on a collection mode detector *Appl. Phys. Lett.* **77** 3496–8
- [33] van der Valk N C J and Planken P C M 2002 Electro-optic detection of subwavelength terahertz spot sizes in the near field of a metal tip *Appl. Phys. Lett.* **81** 1558–60
- [34] Chen H-T, Kersting R and Cho G C 2003 Terahertz imaging with nanometer resolution *Appl. Phys. Lett.* **83** 3009–11
- [35] Mair S, Gompf B and Dressel M 2004 Spatial and spectral behavior of the optical near field studied by a terahertz near-field spectrometer *Appl. Phys. Lett.* **84** 1219–21
- [36] Schade U, Holldack K, Kuste P, Wustefeld G and Hubers H-W 2004 THz near-field imaging employing synchrotron radiation *Appl. Phys. Lett.* **84** 1422–4
- [37] Wang K, Barkan A and Mittleman D M 2004 Propagation effects in apertureless near-field optical antennas *Appl. Phys. Lett.* **84** 305–07
- [38] Wang K, Mittleman D M, van der Valk N C J and Planken P C M 2004 Antenna effects in terahertz apertureless near-field optical microscopy *Appl. Phys. Lett.* **85** 2715–17

- [39] Kawase K, Ogawa Y and Watanabe Y 2003 Non-destructive terahertz imaging of illicit drugs using spectral fingerprints *Opt. Express* **11** 2549–54
- [40] Watanabe Y, Kawase K, Ikari T, Ito H, Ishikawa Y and Minamide H 2003 Component spatial pattern analysis of chemicals using terahertz spectroscopic imaging *Appl. Phys. Lett.* **83** 800–02
- [41] Darmo J, Tamosiunas V, Fasching G, Kröll J, Unterrainer K, Beck M, Giovannini M, Faist J, Kremser C and Debbage P 2004 Imaging with a terahertz quantum cascade laser *Opt. Express* **12** 1879–84
- [42] Chamberlin D R, Robrish P R, Trutna W R, Scalari G, Giovannini M, Ajili L and Faist J 2005 Imaging at 3.4 THz with a quantum-cascade laser *Appl. Opt.* **44** 121–5
- [43] Lu J-Y, Chang H-H, Chen L-J, Tien M-C and Sun C-K 2005 Optoelectronic-based high-efficiency quasi-CW terahertz imaging *IEEE Photonics Tech. Lett.* **17** 2406–08
- [44] Kim S M *et al* 2006 Biomedical terahertz imaging with a quantum cascade laser *Appl. Phys. Lett.* **88** 153903
- [45] Lee A W M, Qin Q, Kumar S, Williams B S, Hu Q and Reno J L 2006 Real-time terahertz imaging over a standoff distance (>25 meters) *Appl. Phys. Lett.* **89** 141125
- [46] Nguyen K L *et al* 2006 Three-dimensional imaging with a terahertz quantum cascade laser *Opt. Express* **14** 2123–9
- [47] Koehler R, Tredicucci A, Beltram F, Beere H E, Linfield E H, Davies A G, Ritchie D A, Iotti R C and Rossi F 2002 Terahertz semiconductor-heterostructure laser *Nature* **417** 156–9
- [48] Rochat M, Ajili L, Willenberg H, Faist J, Beere H, Davies G, Linfield E and Ritchie D 2002 Low-threshold terahertz quantum-cascade lasers *Appl. Phys. Lett.* **81** 1381–3
- [49] Kawase K, Ogawa Y, Minamide H and Ito H 2005 Terahertz parametric sources and imaging applications *Semicond. Sci. Technol.* **20** 258–65
- [50] Yasui T, Yasuda T, Sawanaka K and Araki T 2005 Terahertz paintmeter for noncontact monitoring of thickness and drying progress in paint film *Appl. Opt.* **44** 6849–56
- [51] Lu M, Shen J, Li N, Zhang, Zhang C, Liang L and Xu X 2006 Detection and identification of illicit drugs using terahertz imaging *J. Appl. Phys.* **100** 103104
- [52] Beard M C, Turner G M and Schmuttenmaer C A 2002 Terahertz spectroscopy *J. Phys. Chem. B* **106** 7146–59
- [53] Yujiri L, Shoucri M and Moffa P 2003 Passive millimeter wave imaging *IEEE Micro* **4** 39–50
- [54] Mahon R J, Murphy J A and Lanigan W 2006 Digital holography at millimetre wavelengths *Opt. Commun.* **260** 469–73
- [55] Gunapala S D, Bandara S V, Liu J K, Rafol S B and Mumolo J M 2003 640 × 512 pixel long-wavelength infrared narrowband, multiband, and broadband QWIP focal plane arrays *IEEE Trans. Electron Devices* **50** 2353–60
- [56] van Exter M and Grischkowsky D 1990 Characterization of an optoelectronic terahertz beam system *IEEE Trans. Microw. Theory Tech.* **38** 1684–91
- [57] Jepsen P U, Jacobsen R H and Keiding S R 1996 Generation and detection of terahertz pulses from biased semiconductor antennas *J. Opt. Soc. Am. B* **13** 2424–36
- [58] Han P Y and Zhang X-C 2001 Free-space coherent broadband terahertz time-domain spectroscopy *Meas. Sci. Technol.* **12** 1747–56
- [59] van Exter M, Fattinger C and Grischkowsky D 1989 High-brightness terahertz beams characterized with an ultrafast detector *Appl. Phys. Lett.* **55** 337–9
- [60] Yang K P, Richards P L and Shen Y R 1971 Generation of far-infrared radiation by picosecond light pulses in LiNbO₃ *Appl. Phys. Lett.* **19** 320
- [61] Shen Y R 1976 Far infrared generation by optical mixing *Prog. Quantum Electron.* **4** 207
- [62] Auston D H 1983 Subpicosecond electrooptic shockwaves *Appl. Phys. Lett.* **43** 713
- [63] Hu B B, Zhang X-C, Auston D H and Smith P R 1990 Free space radiation from electro-optic crystals *Appl. Phys. Lett.* **56** 506
- [64] Wu Q and Zhang X-C 1995 Free-space electro-optic sampling of terahertz beams *Appl. Phys. Lett.* **67** 3523–5
- [65] Nahata A, Welington A S and Heinz T F 1996 A wideband coherent terahertz spectroscopy system using optical rectification and electro-optic sampling *Appl. Phys. Lett.* **69** 2321–3
- [66] Winnewisser C, Jepsen P U, Schall M, Schyja V and Helm H 1997 Electro-optic detection of THz radiation in LiTaO₃, LiNbO₃, and ZnTe *Appl. Phys. Lett.* **70** 3069–71
- [67] van Exter M, Fattinger C and Grischkowsky D 1989 Terahertz time-domain spectroscopy of water vapor *Opt. Lett.* **14** 1128–30
- [68] Zhao G, ter Mors M, Wenckebach T and Planken P C M 2002 Terahertz dielectric properties of polystyrene foam *J. Opt. Soc. Am. B* **19** 1476–9
- [69] Planken P C M and Bakker H J 2004 Towards time-resolved THz imaging *Appl. Phys. A* **78** 465–9
- [70] Karpowicz N, Zhong H, Xu J, Lin K-I, Hwang J-S and Zhang X-C 2005 Comparison between pulsed terahertz time-domain imaging and continuous wave terahertz imaging *Semicond. Sci. Technol.* **20** 293–99

- [71] Jepsen P and Fischer B M 2005 Dynamic range in terahertz time-domain transmission and reflection spectroscopy *Opt. Lett.* **30** 29–31
- [72] Pearce J, Jian Z and Mittleman D 2003 Statistics of multiply scattered broadband terahertz pulses *Phys. Rev. Lett.* **91** 043903
- [73] Jian Z, Pearce J and Mittleman D 2003 Characterizing individual scattering events by measuring the amplitude and phase of the electric field diffusing through a random medium *Phys. Rev. Lett.* **91** 033903
- [74] Tani M, Herrmann M and Sakai K 2002 Generation and detection of terahertz pulsed radiation with photoconductive antennas and its application to imaging *Meas. Sci. Technol.* **13** 1739–45
- [75] Mittleman D M, Gupta M, Neelamani R, Baraniuk R G, Rudd J V and Koch M 1999 Recent advances in terahertz imaging *Appl. Phys. B* **68** 1085–94
- [76] Bründermann E, Havenith M, Scalari G, Giovannini M, Faist J, Kunsch J, Mechold L and Abraham M 2006 Turn-key compact high temperature terahertz quantum cascade lasers: imaging and room temperature detection *Opt. Express* **14** 1829–41
- [77] Crawley D, Withington S and Obradovic J 2006 Area-scan camera for terahertz holography *Rev. Sci. Instrum.* **77** 053106
- [78] Creeden D, McCarthy J C, Ketteridge P A, Schunemann P G, Southward T, Komiak J J and Chicklis E P 2007 Compact, high average power, fiber-pumped terahertz source for active real-time imaging of concealed objects *Opt. Express* **15** 6478–83
- [79] Shibuya K, Tani M, Hangyo M, Morikawa O and Kan H 2007 Compact and inexpensive continuous-wave subterahertz imaging system with a fiber-coupled multimode laser diode *Appl. Phys. Lett.* **90** 161127
- [80] Wu Q, Hewitt T D, and Zhang X-C 1996 Two-dimensional electro-optic imaging of THz beams *Appl. Phys. Lett.* **69** 1026–8
- [81] Wu Q, Sun F G, Campbell P and Zhang X-C 1996 Dynamic range of an electro-optic field sensor and its imaging applications *Appl. Phys. Lett.* **68** 3224–6
- [82] Xu J and Zhang X-C 2004 Circular involute stage *Opt. Lett.* **29** 2082–4
- [83] Janke C, Forst M, Nagel M, Kurz H and Bartels A 2005 Asynchronous optical sampling for high-speed characterization of integrated resonant terahertz sensors *Opt. Lett.* **30** 1405–7
- [84] Yasui T, Saneyoshi E and Araki T 2005 Asynchronous optical sampling terahertz time-domain spectroscopy for ultrahigh spectral resolution and rapid data acquisition *Appl. Phys. Lett.* **87** 061101
- [85] Brown M S, Fiechtner G J, Rudd J V, Zimdars D A, Warmuth M and Gord J R 2006 Water-vapor detection using asynchronous THz sampling *Appl. Spectrosc.* **60** 261–5
- [86] Duvillaret L, Garet F and Coutaz J-L 2000 Influence of noise on the characterization of materials by terahertz time-domain spectroscopy *J. Opt. Soc. Am. B* **17** 452–61
- [87] Rudd J V, Johnson J L and Mittleman D M 2000 Quadrupole radiation from terahertz dipole antennas *Opt. Lett.* **25** 1556–8
- [88] Rudd J V, Johnson J L and Mittleman D M 2001 Cross-polarized angular emission patterns from lens-coupled terahertz antennas *J. Opt. Soc. Am. B* **18** 1524–33
- [89] Amer N, Hurlbut W C, Norton B J, Lee Y-S, and Norris T B 2005 Generation of terahertz pulses with arbitrary elliptical polarization *Appl. Phys. Lett.* **87** 221111
- [90] Masson J-B and Gallot G 2006 Terahertz achromatic quarter-wave plate *Opt. Lett.* **31** 265–7
- [91] van der Valk N C J, van der Marel W A M and Planken P C M 2005 Terahertz polarization imaging *Opt. Lett.* **30** 2802–04
- [92] Mittleman D M, Cunningham J, Nuss M C and Geva M 1997 Non-contact semiconductor wafer characterization with the terahertz Hall effect *Appl. Phys. Lett.* **71** 16–18
- [93] Löffler T, Bauer T, Siebert K J, Roskos H G, Fitzgerald A and Czasch S 2001 Terahertz dark-field imaging of biomedical tissue *Opt. Express* **9** 616–21
- [94] Wallace V P, Fitzgerald A J, Pickwell E, Pye R, Taday P F, Flanagan N and Ha T 2006 Terahertz pulsed spectroscopy of human basal cell carcinoma *Appl. Spectrosc.* **60** 1127–1133
- [95] Liu H-B, Chen Y, Bastiaans G J and Zhang X-C 2006 Detection and identification of explosive RDX by THz diffuse reflection spectroscopy *Opt. Express* **14** 415–23
- [96] Guo L, Hu Y, Zhang Y, Zhang C, Chen Y, and Zhang X-C 2006 Vibrational spectrum of γ -HNIW investigated using terahertz time-domain spectroscopy *Opt. Express* **14** 3654–9
- [97] Ino Y, Heroux J B, Mukaiyama T and Kuwata-Gonokami M 2006 Reflection-type pulsed terahertz imaging with a phase-retrieval algorithm *Appl. Phys. Lett.* **88** 041114
- [98] Duvillaret L, Garet F and Coutaz J-L 1999 Highly precise determination of both optical constants and sample thickness in terahertz time-domain spectroscopy *Appl. Opt.* **38** 409–15
- [99] Dorney T D, Baraniuk R G and Mittleman D M 2001 Material parameter estimation using terahertz time-domain spectroscopy *J. Opt. Soc. Am. A* **18** 1562–71

- [100] Zhang L, Zhang Y, Zhang C, Zhao Y and Liu X 2006 Terahertz multiwavelength phase imaging without 2π ambiguity *Opt. Lett.* **31** 3668–70
- [101] Johnson J L, Dorney T D and Mittleman D M 2001 Interferometric imaging with terahertz pulses *IEEE J. Sel. Top. Quantum Electron.* **7** 592–9
- [102] Johnson J L, Dorney T D and Mittleman D M 2001 Enhanced depth resolution in terahertz imaging using phase-shift interferometry *Appl. Phys. Lett.* **78** 835–7
- [103] Ruffin A B, Rudd J V, Whitaker J F, Feng S and Winful H G 1999 Direct observation of the Gouy phase shift with single-cycle terahertz pulses *Phys. Rev. Lett.* **83** 3410–33
- [104] Herman G T 1980 *Image Reconstruction from Projections—The Fundamentals of Computerized Tomography* (New York: Academic)
- [105] Kak A C and Slaney M 1988 *Principles of Computerized Tomographic Imaging* (Piscataway, NJ: IEEE)
- [106] Wang S and Zhang X-C 2004 Pulsed terahertz tomography *J. Phys. D: Appl. Phys.* **37** 1–36
- [107] Rudd J V, Zimdars D and Warmuth M 2000 Compact fiber-pigtailed terahertz imaging system *Proc. SPIE* **3934** 27–35
- [108] Ruffin A B, Decker J, Sanchez-Palencia L, Le Hors L, Whitaker J F, Norris T B and Rudd J V 2001 Time reversal and object reconstruction with single-cycle pulses *Opt. Lett.* **26** 681–3
- [109] Ruffin A B, Rudd J V, Decker J, Sanchez-Palencia L, Le Hors L, Whitaker J F and Norris T B 2002 Time reversal terahertz imaging *IEEE J. Quantum Electron.* **38** 1110–19
- [110] Dorney T D, Symes W W, Baraniuk R G and Mittleman D M 2002 Terahertz multistatic reflection imaging *J. Opt. Soc. Am. A* **19** 1432–42
- [111] Born M and Wolf E 1999 *Principles of Optics* 7th edn (Cambridge, UK: Cambridge University Press)
- [112] Pearce J and Mittleman D M 2002 Defining the Fresnel zone for broadband radiation *Phys. Rev. E* **66** 056602
- [113] Ferguson B, Wang S, Gray D, Abbott D, and Zhang X-C 2002 Towards functional 3D T-ray imaging *Phys. Med. Biol.* **47** 3735–42
- [114] Yin X, Ng B W-H, Ferguson B, Mickan S P and Abbott D 2007 2-D wavelet segmentation in 3-D T-ray tomography *IEEE Sensors J.* **7** 342–3
- [115] Lien Nguyen K *et al* 2006 Three-dimensional imaging with a terahertz quantum cascade laser *Opt. Express* **14** 2123–9
- [116] O'Hara J and Grischkowsky D 2002 Synthetic phased-array terahertz imaging *Opt. Lett.* **27** 1070–2
- [117] Chevillon R A and Grischkowsky D 1995 Time domain terahertz impulse ranging studies *Appl. Phys. Lett.* **67** 1960–2
- [118] Pearce J and Mittleman D M 2002 Scale model experimentation: using terahertz pulses to study light scattering *Phys. Med. Biol.* **47** 3823–30
- [119] Dorney T D, Rossow M, Symes W W and Mittleman D M 2003 Single-cycle terahertz electromagnetic pulses: a new test bed for physical seismic modeling *Geophysics* **68** 308–13
- [120] Federici J F, Gary D, Schulkin B, Huang F, Altan H, Barat R and Zimdars D 2003 Terahertz imaging using an interferometric array *Appl. Phys. Lett.* **83** 2477–9
- [121] Bandyopadhyay A, Stepanov A, Schulkin B, Federici M D, Sengupta A, Gary D, Federici J F, Barat R, Michalopoulou Z-H and Zimdars D 2006 Terahertz interferometric and synthetic aperture imaging *J. Opt. Soc. Am. A* **23** 1168–78
- [122] Lee A W M and Hu Q 2005 Real-time, continuous-wave terahertz imaging by use of a microbolometer focal-plane array *Opt. Lett.* **30** 2563–5
- [123] Herrmann M, Tani M and Sakai K 2000 Display modes in time-resolved terahertz imaging *Japan. J. Appl. Phys. Part 1* **39** 6254–8
- [124] Galvanauskas A, Tellefsen J A, Krotkus A, Oberg M, and Broberg B 1992 Real-time picosecond electro-optic oscilloscope technique using a tunable semiconductor laser *Appl. Phys. Lett.* **60** 145–7
- [125] Dorrer C 2006 Single-shot measurement of the electric field of optical waveforms by use of time magnification and heterodyning *Opt. Lett.* **31** 540–2
- [126] Wilke I, MacLeod A M, Gillespie W A, Berden G, Knippels G M H, and van der Meer A F G 2002 Single-shot electron beam bunch length measurements *Phys. Rev. Lett.* **88** 124801
- [127] Fletcher J R 2002 Distortion and uncertainty in chirped pulse THz spectrometers *Opt. Express* **10** 1425–30
- [128] Jamison S P, Shen J, MacLeod A M, Gillespie W A and Jaroszynski D A 2003 High-temporal-resolution, single-shot characterization of terahertz pulses *Opt. Lett.* **28** 1710–12
- [129] Kim K Y, Yellampalle B, Rodriguez G, Averitt R D, Taylor A J and Glowacki J H 2006 Single-shot, interferometric, high-resolution, terahertz field diagnostic *Appl. Phys. Lett.* **88** 041123
- [130] Siebert K J, Quast H, Leonhardt R, Löffler T, Thomson M, Bauer T, Roskos H G and Czesch S 2002 Continuous-wave all-optoelectronic terahertz imaging *Appl. Phys. Lett.* **80** 3003–05

- [131] Kleine-Ostmann T, Knobloch T, Koch M, Hoffmann S, Breede M, Hofmann M, Hein G, Pierz K, Sperling M and Donhuijsen K 2001 Continuous-wave THz imaging *Electron. Lett.* **37** 1461–3
- [132] Nahata A, Yardley J T and Heinz T F 1999 Free-space electro-optic detection of continuous-wave terahertz radiation *Appl. Phys. Lett.* **75** 2524–6
- [133] Nahata A, Yardley J T and Heinz T F 2002 Two-dimensional imaging of continuous-wave terahertz radiation using electro-optic detection *Appl. Phys. Lett.* **81** 963–5
- [134] Gregory I S, Tribe W R, Baker C, Cole B E, Evans M J, Spencer L, Pepper M and Missous M 2005 Continuous-wave terahertz system with a 60 dB dynamic range *Appl. Phys. Lett.* **86** 204104
- [135] Löffler T, May T, Wäg C a, Alcin A, Hils B and Roskos H G 2007 Continuous-wave terahertz imaging with a hybrid system *Appl. Phys. Lett.* **90** 091111
- [136] Miller A J, Luukanen A and Grossman E N 2004 Micromachined antenna-coupled uncooled microbolometers for terahertz imaging arrays *Proc. SPIE* **5411** 18–24
- [137] Lee A W M, Williams B S, Kumar S, Hu Q and Reno J L 2006 Real-time imaging using a 4.3-THz quantum cascade laser and a 320×240 microbolometer focal-plane array *IEEE Photon. Technol. Lett.* **18** 1415–17
- [138] Fujiwara M, Hirao T, Kawada M, Shibai H, Matsuura S, Kaneda H and Nakagawa M P 2003 Development of a gallium-doped germanium far-infrared photoconductor direct hybrid two-dimensional array *Appl. Opt.* **42** 2166–73
- [139] Kawase K, Shikata J and Ito H 2002 Terahertz wave parametric source *J. Phys. D: Appl. Phys.* **35** R1–14
- [140] Dobroui A, Yamashita M, Ohshima Y N, Morita Y, Otani C and Kawase K 2004 Terahertz imaging system based on a backward-wave oscillator *Appl. Opt.* **43** 5637–46
- [141] Rodriguez-Morales F, Yngvesson K S, Zannoni R, Gerecht E, Gu D, Zhao X, Wadefalk N and Nicholson J J 2006 Development of integrated HEB/MMIC receivers for near-range terahertz imaging *IEEE Trans. Microw. Theory Tech.* **54** 2301–11
- [142] van Exter M and Grischkowsky D 1990 Carrier dynamics of electrons and holes in moderately doped silicon *Phys. Rev. B* **41** 12140–9
- [143] Grischkowsky D, Keiding S, van Exter M and Fattinger C 1990 Far-infrared time-domain spectroscopy with terahertz beams of dielectrics and semiconductors *J. Opt. Soc. Am. B* **7** 2006–15
- [144] Herrmann M, Tani M, Sakai K and Fukasawa R 2002 Terahertz imaging of silicon wafers *J. Appl. Phys.* **91** 1247–50
- [145] Buerstgens F, Kersting R and Chen H-T 2006 Terahertz microscopy of charge carriers in semiconductors *Appl. Phys. Lett.* **88** 112–15
- [146] Karpowicz N, Zhong H, Zhang C, Lin K-I, Hwang J-S, Xu J and Zhang X-C 2005 Compact continuous-wave subterahertz system for inspection applications *Appl. Phys. Lett.* **86** 054105
- [147] Shen Y C, Lo T, Taday P F, Cole B E, Tribe W R and Kemp M C 2005 Detection and identification of explosives using terahertz pulsed spectroscopic imaging *Appl. Phys. Lett.* **86** 241116
- [148] Zhong H, Redo-Sanchez A and Zhang X-C 2006 Identification and classification of chemicals using terahertz reflective spectroscopic focalplane imaging system *Opt. Express* **14** 9130–41
- [149] Pickwell E and Wallace V P 2006 Biomedical applications of terahertz technology *J. Phys. D: Appl. Phys.* **39** R301–10
- [150] Knobloch P *et al* 2002 Medical THz imaging: An investigation of histo-pathological samples *Phys. Med. Biol.* **47** 3875–84
- [151] Woodward R, Cole B E, Wallace V P, Pye R J, Arnone D D, Linfield E H and Pepper M 2002 Terahertz pulse imaging in reflection geometry of human skin cancer and skin tissue *Phys. Med. Biol.* **47** 3853–63
- [152] Pickwell E, Cole B E, Fitzgerald A J, Pepper M and Wallace V P 2004 *In vivo* study of human skin using pulsed terahertz radiation *Phys. Med. Biol.* **49** 1595–607
- [153] Fitzgerald A J, Wallace V P, Jiminez-Linan M, Bobrow L, Pye R J, Purushotham A D and Arnone D D 2006 Terahertz pulsed imaging of human breast tumors *Radiology* **239** 533–40
- [154] Crawley D, Longbottom C, Wallace V P, Cole B, Arnone D and Pepper M 2003 Three-dimensional terahertz pulse imaging of dental tissue *J. Biomed. Opt.* **8** 303–7
- [155] Stringer M R, Lund D N, Foulds A P, Uddin A, Berry E, Miles R E and Davies A G 2005 The analysis of human cortical bone by terahertz time-domain spectroscopy *Phys. Med. Biol.* **50** 3211–19
- [156] Masson J-B, Sauviat M-P and Gallot G 2006 Ionic contrast terahertz time resolved imaging of frog auricular heart muscle electrical activity *Appl. Phys. Lett.* **89** 153904
- [157] Hadjiloucas S, Karatzas L S and Bowen J W 1999 Measurements of leaf water content using terahertz radiation *IEEE Trans. Microw. Theory Tech.* **47** 142–9
- [158] Hadjiloucas S, Galvao R K H and Bowen J W 2002 Analysis of spectroscopic measurements of leaf water content at terahertz frequencies using linear transforms *J. Opt. Soc. Am. A* **19** 2495–509

- [159] Zhong H, Xu J, Xie X, Yuan T, Reightler R, Madaras E and Zhang X-C 2005 Nondestructive defect identification with terahertz time-of-flight tomography *IEEE Sensors J.* **5** 203–07
- [160] Cole A J F E and Taday P F 2005 Nondestructive analysis of tablet coating thicknesses using terahertz pulsed imaging *J. Pharm. Sci.* **94** 177–83
- [161] Taday P F, Bradley I V, Arnone D D and Pepper M 2003 Using terahertz pulse spectroscopy to study the crystalline structure of a drug: A case study of the polymorphs of ranitidine hydrochloride *J. Pharm. Sci.* **92** 831–8
- [162] Zeitler J A, Newnham D A, Taday P F, Threlfall T L, Lancaster R W, Berg R W, Strachan C J, Pepper M, Gordon K C and Rades T 2006 Characterization of temperature-induced phase transitions in five polymorphic forms of sulfathiazole by terahertz pulsed spectroscopy and differential scanning calorimetry *J. Pharm. Sci.* **95** 2486–98
- [163] Brucherseifer M, Bolivar P H, Klingenberg H and Kurz H 2001 Angle-dependent THz tomography—characterization of thin ceramic oxide films for fuel cell applications *Appl. Phys. B* **72** 361–6
- [164] Geltner I, Hashimshony D and Zigler A 2002 Detection and electrical characterization of hidden layers using time-domain analysis of terahertz reflections *J. Appl. Phys.* **92** 203–06
- [165] Yasuda T, Yasui T, Araki T and Abraham E 2006 Real-time two-dimensional terahertz tomography of moving objects *Opt. Commun.* **267** 128–36
- [166] Koch M, Hunsche S, Schuacher P, Nuss M C, Feldmann J and Fromm J 1998 THz-imaging: a new method for density mapping of wood *Wood Sci. Technol.* **32** 421–7
- [167] Betzig E, Trautman J K, Harris T D, Weiner J S and Kostelak R L 1991 Breaking the diffraction barrier - optical microscopy on a nanometric scale *Science* **251** 1468–70
- [168] Hunsche S, Mittleman D M, Koch M and Nuss M C 1998 New dimensions in T-ray imaging *IEICE Trans. Electron.* **E81-C** 269
- [169] Keilmann F 1995 FIR microscopy *Infrared Phys. Tech.* **36** 217–24
- [170] Mitrofanov O, Brener I, Wanke M C, Ruel R R, Wynn J D, Bruce A J and Federici J 2000 Near-field microscope probe for far infrared time domain measurements *Appl. Phys. Lett.* **77** 591–3
- [171] Mitrofanov O, Lee M, Hsu J W P, Brener I, Harel R, Federici J, Wynn J D, Pfeiffer L N and West K W 2001 Collection-mode near-field imaging with 0.5-THz pulses *IEEE J. Sel. Top. Quantum Electron.* **7** 600–07
- [172] Chen Q and Zhang X-C 2001 Semiconductor dynamic aperture for near-field terahertz wave imaging *IEEE J. Sel. Top. Quantum Electron.* **7** 608–14
- [173] Gompf B, Gebert N, Heer H and Dressel M 2007 Polarization contrast terahertz-near-field imaging of anisotropic conductors *Appl. Phys. Lett.* **90** 082104
- [174] Bethe H A 1944 Theory of diffraction by small holes *Phys. Rev.* **66** 163–82
- [175] Mitrofanov O, Lee M, Hsu J W P, Pfeiffer L N, West K W, Wynn J D and Federici J 2001 Terahertz pulse propagation through small apertures *Appl. Phys. Lett.* **79** 907–09
- [176] Cao H, Agrawal A and Nahata A 2005 Controlling the transmission resonance lineshape of a single subwavelength aperture *Opt. Express* **13** 763–9
- [177] Ishihara K, Ikari T, Minamide H, Shikata J-i, Ohashi K, Yokoyama H and Ito H 2005 Terahertz near-field imaging using enhanced transmission through a single subwavelength aperture *Japan. J. Appl. Phys.* **44** L929–31
- [178] Ishihara K, Ohashi K, Ikari T, Minamide H, Yokoyama H, Shikata J, and Ito H 2006 Terahertz wave near-field imaging with subwavelength resolution using surface-wave-assisted bow-tie aperture *Appl. Phys. Lett.* **89** 201120
- [179] Nahata A and Heinz T F 1996 Reshaping of freely propagating terahertz pulses by diffraction *IEEE J. Sel. Top. Quantum Electron.* **2** 701–08
- [180] McGowan R W, Gallot G and Grischkowsky D 1999 Propagation of ultrawideband short pulses of terahertz radiation through submillimeter-diameter circular waveguides *Opt. Lett.* **24** 1431–3
- [181] Inouye Y and Kawata S 1994 Near-field scanning optical microscope with a metallic probe tip *Opt. Lett.* **19** 159–61
- [182] Zenhausern F, O'Boyle M P and Wickramasinghe H K 1994 Apertureless near-field optical microscope *Appl. Phys. Lett.* **65** 1623
- [183] Zenhausern F, Martin Y and Wickramasinghe H K 1995 Scanning interferometric apertureless microscopy—optical imaging at 10 Angstrom resolution *Science* **269** 1083
- [184] Grober R D, Schoelkopf R J and Prober D E 1997 Optical antenna: towards a unity efficiency near-field optical probe *Appl. Phys. Lett.* **70** 1354
- [185] Knoll B and Keilmann F 1999 Near-field probing of vibrational absorption for chemical microscopy *Nature* **399** 134

- [186] Martin Y C and Wickramasinghe H K 2002 Resolution test for apertureless near-field optical microscopy *J. Appl. Phys.* **91** 3363–8
- [187] Knoll B, Keilmann F, Kramer A and Guckenberger R 1997 Contrast of microwave near-field microscopy *Appl. Phys. Lett.* **70** 2667–9
- [188] van der Valk N C J, Wenckebach T and Planken P C M 2004 Full mathematical description of electro-optic detection in optically isotropic crystals *J. Opt. Soc. Am. B* **21** 622–31
- [189] Planken P C M, van Rijmenam C E W M and Schouten R N 2005 Opto-electronic pulsed THz systems *Semicond. Sci. Technol.* **20** S121–7
- [190] Aigouy L, Andréani F X, Boccara A C, Rivoal J C, Porto J A, Carminati R, Greffet J-J and Mégy R 2000 Near-field optical spectroscopy using an incoherent light source *Appl. Phys. Lett.* **76** 397–9
- [191] Seidel J, Grafström S, Loppacher C, Trogisch S, Schlaphof F and Eng L M 2001 Near-field spectroscopy with white-light illumination *Appl. Phys. Lett.* **79** 2291–3
- [192] Wang K and Mittleman D M 2004 Metal wires for terahertz wave guiding *Nature* **432** 376–9
- [193] Wang K and Mittleman D M 2005 Guided propagation of terahertz pulses on metal wires *J. Opt. Soc. Am. B* **22** 2001–8
- [194] Stutzman W L and Thiele G A 1981 *Antenna theory and design* (New York: Wiley)
- [195] Chen H-T, Kraatz S, Cho G C and Kersting R 2004 Identification of a resonant imaging process in apertureless near-field microscopy *Phys. Rev. Lett.* **93** 267401
- [196] Ikushima K, Sakuma H and Komiyama S 2003 A highly sensitive scanning far-infrared microscope with quantum Hall detectors *Rev. Sci. Instrum.* **74** 4209–11
- [197] Ikushima K, Sakuma H, Komiyama S and Hirakawa K 2004 Imaging of cyclotron emission from edge channels in quantum Hall conductors *Phys. Rev. Lett.* **93** 146804
- [198] Brener I, Dykaar D, Frommer A, Pfeiffer L N, Lopata J, Wynn J, West K and Nuss M C 1996 Terahertz emission from electric field singularities in biased semiconductors *Opt. Lett.* **21** 1924–6
- [199] Shikii S, Kondo T, Yamashita M, Tonouchi M, Hangyo M, Tani M and Sakai K 1999 Observation of supercurrent distribution in $\text{YBa}_2\text{Cu}_3\text{O}_{7-\delta}$ thin films using THz radiation excited with femtosecond laser pulses *Appl. Phys. Lett.* **74** 1317–19
- [200] Tonouchi M, Yamashita M and Hangyo M 2000 Terahertz radiation imaging of supercurrent distribution in vortex-penetrated $\text{YBa}_2\text{Cu}_3\text{O}_{7-\delta}$ thin film strips *J. Appl. Phys.* **87** 7366–75
- [201] Kiwa T, Tonouchi M, Yamashita M and Kawase K 2003 Laser terahertz-emission microscope for inspecting electrical faults in integrated circuits *Opt. Lett.* **28** 2058–60
- [202] Yamashita M, Kawase K, Otani C, Kiwa T and Tonouchi M 2005 Imaging of large-scale integrated circuits using laser terahertz emission microscopy *Opt. Express* **13** 115–20
- [203] Kiwa T, Tsukada K, Suzuki M, Tonouchi M, Migitaka S, and Yokosawa K 2005 Laser terahertz emission system to investigate hydrogen gas sensors *Appl. Phys. Lett.* **86** 261102
- [204] Klein N, Lahl P, Poppe U, Kadlec F and Kuzel P 2005 A metal-dielectric antenna for terahertz near-field imaging *J. Appl. Phys.* **98** 014910